

Finite Operator Learning: Bridging Neural Operators and Numerical Methods for Efficient Parametric Solution and Optimization of PDEs

Shahed Rezaei^{1,*}, Reza Najian Asl^{2,*}, Kianoosh Taghikhani¹, Ahmad Moeineddin³,
Michael Kaliske³, Markus Apel¹

¹*ACCESS e.V., Intzestr. 5, 52072 Aachen, Germany*

²*Chair of Structural Analysis, Technical University of Munich, Arcisstr. 21, 80333 München, Germany*

³*Institute for Structural Analysis, Technische Universität Dresden,
Georg-Schumann-Str. 7, 01187 Dresden, Germany*

* *corresponding authors: s.rezaei@access-technology.de, reza.najian-asl@tum.de*¹

arXiv:2407.04157v1 [cs.CE] 4 Jul 2024

Abstract

We introduce a method that combines neural operators, physics-informed machine learning, and standard numerical methods for solving PDEs. The proposed approach extends each of the aforementioned methods and unifies them within a single framework. We can parametrically solve partial differential equations in a data-free manner and provide accurate sensitivities, meaning the derivatives of the solution space with respect to the design space. These capabilities enable gradient-based optimization without the typical sensitivity analysis costs, unlike adjoint methods that scale directly with the number of response functions. Our Finite Operator Learning (FOL) approach uses an uncomplicated feed-forward neural network model to directly map the discrete design space (i.e. parametric input space) to the discrete solution space (i.e. finite number of sensor points in the arbitrary shape domain) ensuring compliance with physical laws by designing them into loss functions. The discretized governing equations, as well as the design and solution spaces, can be derived from any well-established numerical techniques. In this work, we employ the Finite Element Method (FEM) to approximate fields and their spatial derivatives. Subsequently, we conduct Sobolev training to minimize a multi-objective loss function, which includes the discretized weak form of the energy functional, boundary conditions violations, and the stationarity of the residuals with respect to the design variables. Our study focuses on the steady-state heat equation within heterogeneous materials that exhibits significant phase contrast and possibly temperature-dependent conductivity. The network's tangent matrix is directly used for gradient-based optimization to improve the microstructure's heat transfer characteristics. To efficiently parameterize the spatially varying conductivity field as a design field, we utilize Fourier-based parameterization. This method enables us to generate complex microstructures using a limited number of amplitudes and frequencies. When optimization and parametric learning are not of interest, our technique simplifies to an efficient matrix-free PDE solver that can compete with standard available solvers. This is demonstrated by solving a nonlinear thermal PDE on a complex 3D geometry discretized with an unstructured mesh.

Keywords: Neural operators, Physics-informed neural networks, Sobolev training, Adjoint-free sensitivity analysis, Matrix-free PDE solver.

¹The first two authors contributed equally to this work.

1. Introduction

Simulations of physical phenomena are recognized as the third pillar of science [1]. While we focus on developing new models to accurately describe reality, a pressing and arguably more significant challenge lies in the efficient (i.e., rapid) and precise (i.e., high-accuracy) evaluation of these models for optimization purposes. This challenge is particularly noteworthy in the context of developing digital twins or shadows [2].

1.1. Current trends in computational methods

Over the past decades, numerous numerical techniques have been developed for various applications, gaining significant attention for their remarkable predictive capabilities in solving model equations. Among them, one can name the finite difference method (FDM), finite volume method (FVM), and FEM [3, 4]. Despite their great predictive abilities, these methods remain time-consuming in recent applications including multiphysics and coupled sets of nonlinear equations [5, 6]. Another issue is that these methods cannot solve the equations in a parametric way. In other words, by any slight change in the input parameters, one has to repeat the calculations.

Machine learning (ML) techniques present a promising solution for overcoming the previously mentioned challenges, offering a considerable speed advantage over classical solvers once effectively trained [7]. The efficiency of ML algorithms holds particular relevance in multi-scaling analysis (refer to [8, 9] and references therein). While training time is a factor, it represents a one-time investment compared to the substantial speedup achieved [10].

To ensure reliability, adequate training data encompassing relevant scenarios is essential. Moreover, integrating well-established physical constraints enhances prediction capabilities [11]. Among various options, a well-established method to perform the latter task is the physics-informed neural networks (PINNs) as introduced by Raissi et al. [12]. Additionally, in scenarios where the underlying physics of the problem is completely known, it becomes possible to train the neural network without any initial data [11, 12, 13]. Comparable studies, such as the work by Sirignano and Spiliopoulos [14], propose methods like the deep Galerkin approach, which leverages deep neural networks to approximate solutions for high-dimensional partial differential equations. Markidis [15] demonstrated that the standard version of PINNs can quickly converge for low-frequency components of the solution, while accurately capturing high-frequency components demands a longer training period. In response to these shortcomings, extensions to the PINN framework have been proposed. Some advancements are rooted in the domain decomposition method [16, 17, 18], while others focus on novel architectures and adaptive weights to augment accuracy [19, 20, 21]. Recent investigations have proposed the reduction of differential orders to construct loss functions and utilizing the energy form of equations [11, 22, 23, 24].

1.2. Idea behind parametric learning and neural operators

Despite the above progress, one main issue with solving partial differential equations using standard PINNs is that the solutions are still limited to specific boundary value problems. Furthermore, in many engineering applications, the training time of the PINN for the forward problem, even with the most advanced optimizers and enhancements, cannot compete with those of more established numerical methods such as the finite element method. Nevertheless,

thanks to the flexibility and interpolation power of neural networks, they have the potential to be extended and trained on a wider range of input parameters. Here, we review two main strategies for parametric learning of differential equations.

The first potential approach to generalize solutions obtained from neural networks is to employ transfer learning algorithms. This involves transferring pre-trained hyperparameters of a neural network to initialize the NN for the new domain [11, 25, 26, 27, 28]. Another strategy involves leveraging operator learning, which entails mapping two function spaces to each other. Some well-established methods for operator learning include but are not limited to DeepOnet [29] and Fourier Neural Operator [30]. For an in-depth exploration of this topic, refer to [3, 31].

The concept of PINN can also be integrated with Operator Learning (OL) to broaden the range of parameters for which the network can predict solutions. In [32], the authors utilized a physics-informed DeepONet framework to solve engineering problems. Several contributions utilizing physics-driven operator learning are outlined below. Koric and Abueidda [33] investigated data-driven and physics-based DeepONets for solving heat conduction equations incorporating a parametric source term. Zhu et al. [34] utilized a convolutional encoder-decoder neural network to train physics-constrained deep learning models without labeled data. Gao et al. [35] introduce a novel physics-constrained CNN learning architecture based on elliptic coordinate mapping, facilitating coordinate transforms between irregular physical domains and regular reference domains. Zhang and Gu [36] introduce a physics-informed neural network tailored for analyzing digital materials, training the NN without labeled ground data using minimum energy criteria. Li et al. [37] propose a physics-informed operator neural network framework predicting dynamic responses of systems governed by gradient flows of free-energy functionals. For achieving higher efficiency and potentially larger accuracy, Kontolati et al. [38] suggest mapping high-dimensional datasets to a low-dimensional latent space of salient features using suitable autoencoders and pre-trained decoders. Zhang and Garikipati [39] present encoder-decoder architectures to learn how to solve differential equations in weak form, capable of generalizing across domains, boundary conditions, and coefficients.

A recent trend in the literature aims to approximate derivatives more efficiently using classical numerical approaches. This methodology transforms the loss function from a differential equation to an algebraic one. However, it is important to note that this approach may introduce discretization errors, influencing the network’s outcomes. Fuhg et al. [40] introduced the deep convolutional Ritz method, a parametric PDE solver relying on minimizing energy functionals. Additionally, studies by Ren et al. [41], Zhao et al. [42], and Zhang et al. [43] explore physics-driven convolutional neural networks based on finite difference and volume methods. In their work [44], authors proposed a framework for incorporating conservation constraints into neural networks, employing common discretization schemes like the trapezoidal rule for integral operators. Moreover, investigations by Phillips et al. [45] showcase a novel approach leveraging artificial intelligence software libraries to replicate the process of solving partial differential equations using standard numerical methods like finite volume or finite element schemes.

1.3. Inverse design and optimization through ML

Besides the prediction purposes of numerical simulations, a major goal and subsequent question is how to design the structure or material based on specific objectives (i.e., desired constraints). Strategically designing material microstructures can optimize properties such as strength, and conductivity, resulting in lightweight, robust, and thermally stable materials. However, this optimization process is complex due to the vast design space, high simulation costs, and the expense of sensitivity analysis. Researchers have explored the applicability of

neural networks (NNs) to numerical design analysis and optimization in various ways. For example, [46, 47, 48, 49] employed NNs in a fully data-driven manner, while [50, 51, 52, 53] utilized them for parameterization and as PDE solvers. For a critical review of the research on the application of artificial intelligence in topology optimization, the reader is encouraged to consult [54].

In PDE-constrained optimization, there are primarily two approaches used to solve the optimization problem: the Simultaneous Analysis and Design (SAND) approach and the Nested Analysis and Design (NAND) approach [55]. In the SAND approach, state and design variables are updated simultaneously, offering a richer exploration space but with high computational demands and non-physically feasible intermediate solutions. In contrast, the NAND technique fully satisfies state equations within a nested loop, producing valid intermediate designs and is more suitable for large-scale problems. Consequently, NAND is preferred for PDE-constrained gradient-based optimization. However, deep neural networks favor the SAND approach due to the ease of integrating optimization responses into the loss function, along with PDE and boundary condition losses.

Besides the standard machine learning framework, research has also begun on combining ideas from PINNs into optimization problems. Zhang et al. [56] present a weak-form PINN for the topology optimization of heterogeneous materials, addressing the spatial discontinuity challenges. The authors also integrate loss terms with optimization objectives, which eliminates the need for pre-trained surrogate models or analytical sensitivity derivations. Mowlavi and Kamrin [57] combined PINN with topology optimization to detect hidden geometries in the noninvasive imaging processes. Their approach allows the network to predict physical fields such as displacements, stresses, and the density field. Tillmann et al. [58] incorporated the free-form deformation parametrization into PINNs to enable rapid design space exploration in fluid shape optimization. While they examined the network’s performance in predicting physical fields, they did not address the network’s output-to-input gradients, the quality of which is crucial for gradient-based shape optimization. Jeong et al. [59] provided a framework for structural topology optimization using two PINNs. First, the Deep Energy Method (DEM) is trained to approximate the deformation of the design domain. Then, the sensitivity-analysis PINN (S-PINN) is used to differentiate the objective function with respect to (w.r.t) design variables using automatic differentiation. He et al. [50] explored a specific class of topology optimization using the deep energy method for predicting the displacement field. In this case, structural compliance is minimized, which is self-adjoint. Consequently, sensitivities are readily available.

In summary, despite the significant contributions reviewed above, neural network-based optimal designs perform similarly to fully FEM-based optimal designs. However, to the best of our knowledge, researchers report higher costs by utilizing physics-informed DL methods. This is primarily because the SAND approach is often followed, as it simplifies the integration of the optimization problem into the loss function of the state problem. For PDE-constrained gradient-based optimization, however, NAND is preferred over SAND due to its lower computational costs and ability to produce valid intermediate solutions. Therefore, we formulate and perform optimization using the NAND mode, see Section 2.

1.4. Our contribution

Inspired by discretization techniques, along with discrete weak formulation, we propose a novel approach for physics-based operator learning applicable to design analysis and optimization. Our proposed approach, coined as Finite Operator Learning (FOL), parametrically solves

discretized Partial Differential Equations (PDEs) and provides accurate solution-to-design sensitivity. In this framework, *finite* indicates that the discrete solution field is hardwired to the network architecture and constrained through the physical loss function formulated using classical numerical methods for PDEs. Consequently, the network is informed about the mesh, and no coordinates are directly input into it. Mathematically, FOL can map any discrete design or parameter space (input layer) to any discrete solution space (output layer) while satisfying physical constraints, specifically minimum energy, zero residuals, and the stationarity of these residuals w.r.t the design variables. The latter results in the so-called Sobolev training [60, 61, 62, 63], where the network’s output-to-input (solution-to-design) sensitivities are incorporated into the loss function to meet specific criteria. The proposed framework is data-free and in specific cases, the method also reduces to a matrix-free nonlinear solver.

This work is based on feed-forward neural networks, where the outputs are FEM nodal unknowns, and the inputs can be any variables that influence the solution explicitly or implicitly through a parametrization operator. Here, we demonstrate the applicability of FOL to the analysis and optimization of steady-state heat equations. Nodal conductivities are used directly as design variables by employing them as network inputs and indirectly by using the Fourier parametrization technique [64, 65]. The latter efficiently parametrizes spatially varying design fields using a limited number of amplitudes and frequencies. Typically, frequencies are fixed based on the desired scale of features, while amplitudes are subject to optimization. As a result, FOL maps amplitudes of the Fourier-based design space to the solution space, significantly reducing the computational complexity of the training. This reduction in complexity is one of the novelties of this work. Fig. 1 schematically illustrates the structure and features of FOL.

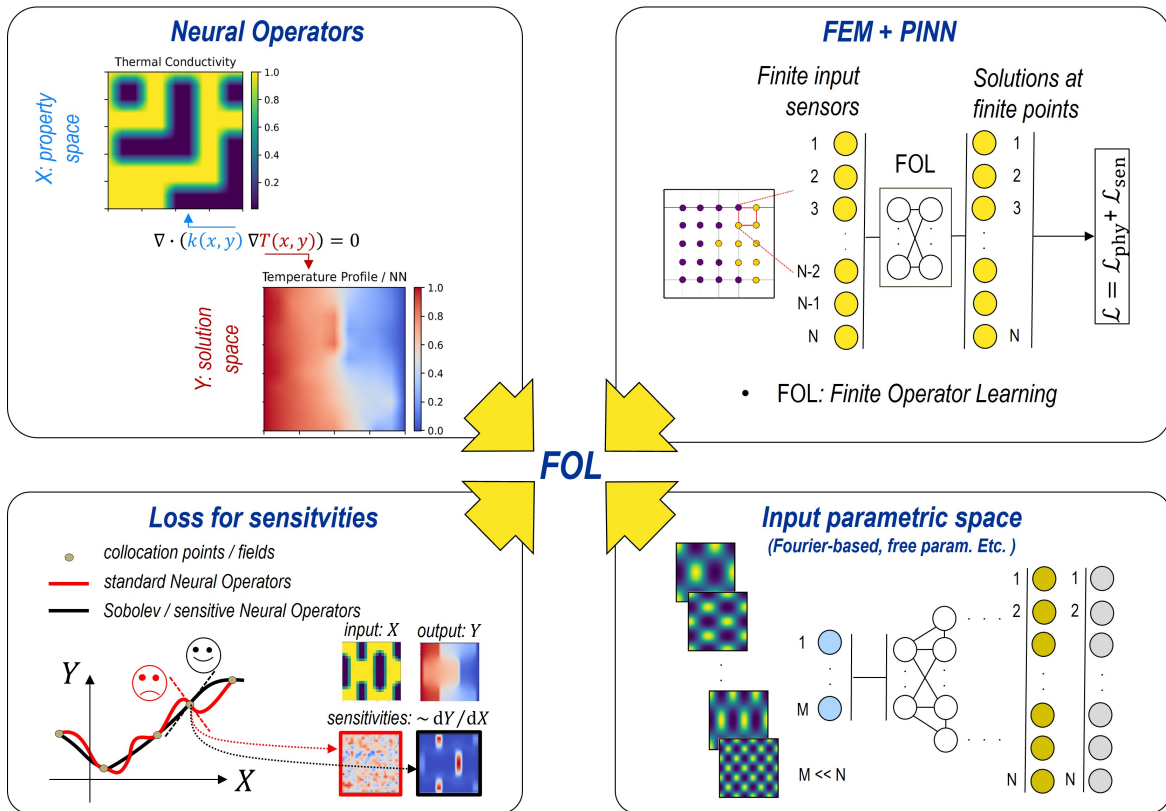


Figure 1: The Finite Operator Learning framework integrates classical numerical solvers and modern machine learning into a unified approach, providing reliable predictions for both forward and optimization problems.

The rest of this paper is structured as follows. Section 2 presents the design analysis and optimization problem, including the heat transfer governing equations, Fourier parametrization, and gradient-based optimization. In Section 3, we present mathematically FOL as a physics-based operator learning for primal and sensitivity analysis. Sections 4.2 and 4.3 critically examine the performance of the proposed framework compared to the reference method, FEM, in terms of the accuracy of predicted primals and gradients, optimality, and computational cost. In Section 4.4 we discuss the potential of the FOL as a new and efficient nonlinear solver for 3D problems. Finally, we conclude with our achievements and discuss potential future developments.

2. Problem definition

In this work, the design problem is formulated using the NAND approach (see 1.3) which involves three key steps: analysis of the underlying governing equations, design parameterization, and design variation, typically aimed at optimization. Each of these steps will be thoroughly examined in the following subsections. Mathematically, the goal is to optimize a function J that depends on physical design variables, denoted by k , both directly and indirectly through state variables, denoted by T . These state variables are governed by a set of partial differential equations represented by \mathcal{R} . We initially formulate the problem in its continuous form and subsequently apply the finite element technique to solve it numerically. The problem is defined as:

$$\begin{aligned} \min_{c \in \mathbb{R}} \quad & J(k, T), \\ \text{subject to} \quad & \mathcal{A}(k, c) = 0, \quad k \in \mathbb{R}, \\ & \mathcal{R}(k, T) = 0, \quad \text{in } \Omega. \end{aligned} \tag{1}$$

In the stated formulation, parametrization is addressed by the operator \mathcal{A} . This operator functionally maps the true control variables, represented as c , to the physical design variables (k). We also note that if no specific parametrization is involved, the parametrization operator acts as the identity, resulting in $c = k$.

2.1. Governing equations

We explore a well-established problem of steady-state diffusion in a heterogeneous solid. Moreover, we intend to optimize the conductivity distribution for a given desired property of the microstructure. It is worth noting that the same derivation principles can be applied to investigate analogous fields such as electrostatics, electric conduction, or magnetostatic problems. See also the Poisson Problem. Additionally, this approach extends to fields like chemical diffusion [66] (under some assumptions) and Darcy flow. In this context, the heat flux \mathbf{q} is defined based on Fourier's law

$$\mathbf{q} = -k(x, y, z) \nabla T. \tag{2}$$

Here $k(x, y, z)$ is the phase-dependent heat conductivity coefficient. The governing equation for this problem is based on the heat balance which reads

$$\mathcal{R}(k, T) = \text{div}(\mathbf{q}) + Q = 0 \quad \text{in } \Omega, \tag{3}$$

$$T = \bar{T} \quad \text{on } \Gamma_D, \tag{4}$$

$$\mathbf{q} \cdot \mathbf{n} = q_n = \bar{q} \quad \text{on } \Gamma_N. \tag{5}$$

In the above relations, Q is the heat source term. Moreover, Dirichlet and Neumann boundary conditions are introduced in Eq. 4 and Eq. 9, respectively. By introducing δT as a test function and with integration by parts, the weak form of the steady-state diffusion problem reads

$$\int_{\Omega} k(x, y, z) \nabla^T T \delta(\nabla T) dV + \int_{\Gamma_N} \bar{q} \delta T dA - \int_{\Omega} Q \delta T dV = 0. \quad (6)$$

Finally, using the standard finite element method, the discrete residual form of the steady-state diffusion equation can be expressed as:

$$\mathbf{r}(\mathbf{k}, \mathbf{T}) = \mathbf{K}(\mathbf{k}) \mathbf{T} - \mathbf{f} = \mathbf{0} \quad \mathbf{r} \in \mathbb{R}^r, \text{ in } \Omega, \quad (7)$$

$$\mathbf{T} = \bar{T} \quad \text{on } \Gamma_D, \quad (8)$$

$$\mathbf{q} \cdot \mathbf{n} = q_n = \bar{q} \quad \text{on } \Gamma_N. \quad (9)$$

Here, \mathbf{K} represents the stiffness matrix, \mathbf{r} is the residual vector, \mathbf{T} is the solution vector, and \mathbf{f} denotes the force vector. It is important to note that the heat conductivity field, represented by \mathbf{k} , is also discretized at nodes and serves as the physical design variable subject to change and optimization. For the derivation of the residual form, please refer to the Appendix A.

2.2. Parameterization

A key aspect of parametric learning and optimization is the underlying parameter space. An efficient design space should be capable of exploring complex designs while avoiding unnecessary design parameters. In this regard, there are two main approaches in the literature: filter-based techniques, such as implicit and explicit filtering [67], and filter-free techniques, such as CAD-based [68] and Fourier-based [69] parameterizations. While the first approach is well-established and widely used in practice, the second approach gains increasing attention due to its significant reduction of the design variables, making it computationally more efficient.

In the following, we begin with a parameterization-free representation of the discrete conductivity field, which varies spatially. We then introduce the Fourier transform as a robust method to control this spatially varying physical space using a limited number of variables.

2.2.1. Parameterization-free design space

This study focuses on a two-phase material where each phase's properties remain constant. However, the microstructure's morphology is altered, allowing for arbitrary shapes and volume fraction ratios.

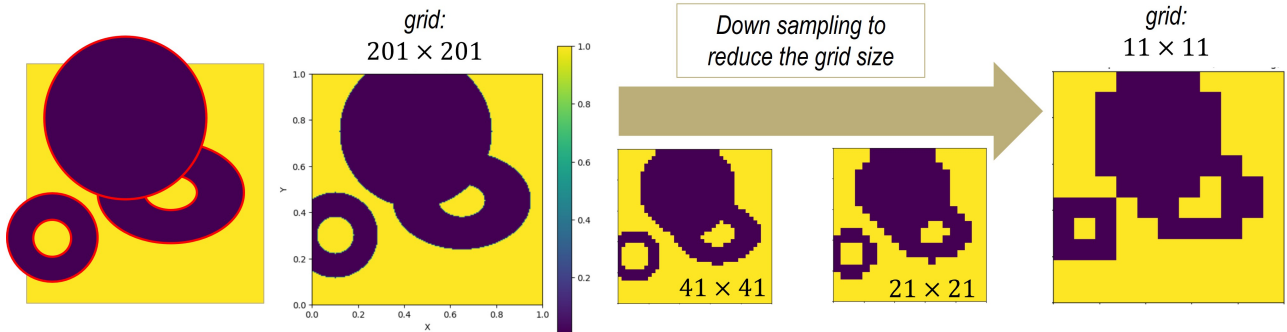


Figure 2: Downsampling the grid size involves using convolutional layers combined with max-pooling, resulting in a reduced space of $11 \times 11 = 121$ grid points. The training will be conducted based on an 11 by 11 grid size. The value of thermal conductivity lies between $k_{min} = 0.01$ and $k_{max} = 1.0$ [W/m^2].

Based on experience with composite materials, we propose the following strategy for creating samples: 1) select a set of random center points based on a user-defined number, 2) choose random values for the inner radius, outer radius, and rotation angle of the ellipse, with ranges for these values all user-defined, and 3) assign a (low) conductivity value to the grid nodes inside the defined region. We then perform a downsampling process via max-pooling on the high-resolution microstructure images, as depicted in Fig. 2. For more details on down and upsampling strategy, see [70].

2.2.2. Fourier-based parameterization

Given our interest in periodic design and achieving higher resolution for the solution space without any downsampling, we utilize the Fourier transform method. In short, the idea is to combine various frequencies of sinusoidal and cosinusoidal functions to describe spatially varying fields [69], here the heat conductivity. As a result, and as depicted in Fig. 3, we can reduce the number of inputs to M desired combinations of frequencies, which is usually a much lower number than the number of degrees of freedom in the system, denoted by N .

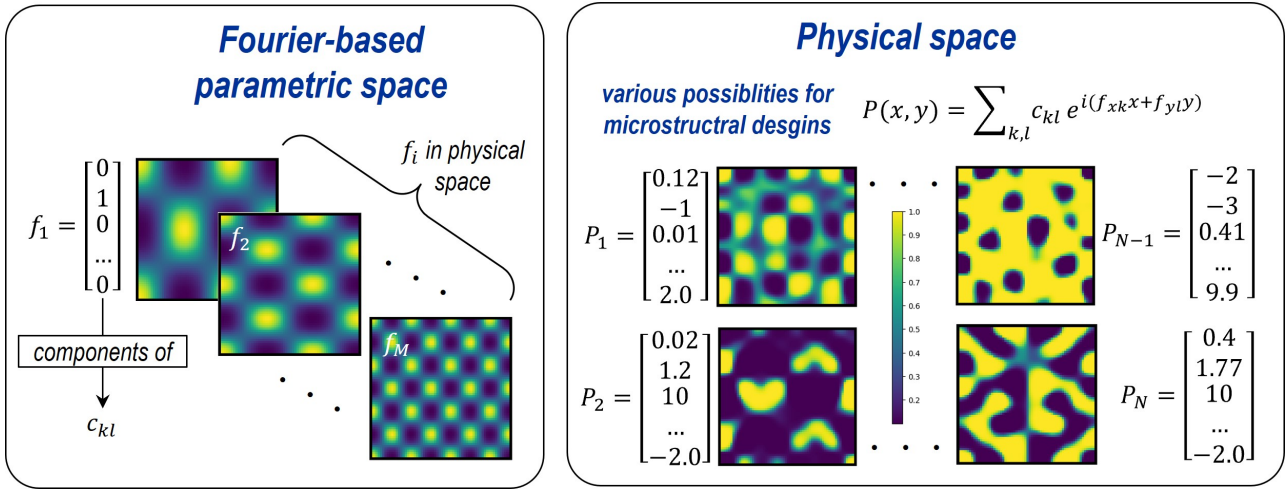


Figure 3: Fourier-based parameterization helps to decrease the input parametric space dimension.

The Fourier-based function for representation of the conductivity map in a 2D setting has the following form through a combination of sine and cosine functions

$$k_f(x, y) = \sum_i^{n_{sum}} [A_i \sin(f_{x,i} x) \cos(f_{y,i} y) + B_i \cos(f_{x,i} x) \sin(f_{y,i} y) + C_i \sin(f_{x,i} x) \sin(f_{y,i} y) + D_i \cos(f_{x,i} x) \cos(f_{y,i} y)]. \quad (10)$$

In Eq. 10, and $\mathbf{x} = (x, y)^T$, $\{A_i, B_i, C_i, D_i\}$ represents the amplitudes of the corresponding frequency number and $\{f_{x,i}, f_{y,i}\}$ represents the frequency in the x - and y -direction. Finally, we pass the property function E_f through a so-called sigmoidal projection to have more realistic and interesting characteristics for the microstructure

$$k(x, y) = (k_{max} - k_{min}) \cdot \text{Sigmoid}(\beta(k_f - 0.5)) + E_{min}. \quad (11)$$

With the above projection, we ensure that the value of thermal conductivity lies between $k_{min} = 0.01$ and $k_{max} = 1.0$ [W/m^2]. With the β parameter, one can also control the transition between the two phases, which is set to $\beta = 5$ for the samples in this study. Some of the main modes, as well as possible samples that this approach can process, are shown in the lower part of Fig. 3.

2.3. Gradient-based optimization

In this section, we revisit the problem defined in Eq. 1 and expand our discussion to address constrained optimization problems. Consequently, the optimization problem in its discrete form is presented as

$$\begin{aligned} \min_{\mathbf{c}} \quad & J(\mathbf{k}, \mathbf{T}), \\ \text{subject to} \quad & \mathbf{k} = \mathbf{A} \mathbf{c}, \\ & \mathbf{r} = \mathbf{K}(\mathbf{k}) \mathbf{T} - \mathbf{f} = \mathbf{0}, \\ & h_j = 0, \quad j = 1, \dots, m_h, \\ & g_j \leq 0, \quad j = 1, \dots, m_g. \end{aligned} \quad (12)$$

In this formulation, \mathbf{h} and \mathbf{g} represent the vectors of equality and inequality constraints, respectively. To find the optimum solution, we follow first-order optimization with an adapted version of Rosen's gradient projection technique [71]. This method iteratively adjusts the true control variables based on the projected gradients, ensuring that each step moves towards a reduction in the objective function while satisfying all imposed constraints. This approach is detailed as

$${}^{k+1}\mathbf{c} = {}^k\mathbf{c} - \alpha \underbrace{\left[\mathbf{I} - \mathbf{P} (\mathbf{P}^T \mathbf{P})^{-1} \mathbf{P}^T \right]}_{\text{projection}} \frac{dJ}{d\mathbf{c}} - \overbrace{\left[\mathbf{P} (\mathbf{P}^T \mathbf{P})^{-1} \right]}^{\text{correction}} \mathbf{g}^a, \quad (13)$$

where α is the projection step size. The matrix $\mathbf{P} \in \mathbb{R}^c \times \mathbb{R}^a$ contains the gradients $d\mathbf{g}^a/d\mathbf{c}$ in a column-wise arrangement, with $\mathbf{g}^a \in \mathbb{R}^a$ being the vector of active constraints. The update rule equation above includes both a projection and a correction term. The projection term projects the steepest descent direction onto a subspace tangent to the active constraints, while the correction term ensures that the update direction remains feasible in the presence of nonlinear constraints.

To update the design variables detailed in Eq. 13, it is necessary to determine the gradients of both the objective function and the constraints with respect to the true design variables. These calculations must also comply with the underlying physical governing equations that characterize the system. By employing the chain rule for differentiation, the gradients of any state-dependent function, such as the objective function, can be expressed as

$$\frac{dJ}{d\mathbf{c}} = \left(\frac{\partial J}{\partial \mathbf{T}} \frac{d\mathbf{T}}{d\mathbf{k}} + \frac{\partial J}{\partial \mathbf{k}} \right) \frac{d\mathbf{k}}{d\mathbf{c}}. \quad (14)$$

While the partial derivatives can often be computed using analytical or automatic differentiation methods, computing the total derivatives involves differentiating both the underlying governing physical equations and the parametrization equations, as per

$$\frac{d\mathbf{r}}{d\mathbf{k}} = \frac{\partial \mathbf{r}}{\partial \mathbf{T}} \frac{d\mathbf{T}}{d\mathbf{k}} + \frac{\partial \mathbf{r}}{\partial \mathbf{k}} = \mathbf{0}, \text{ then } \frac{d\mathbf{T}}{d\mathbf{k}} = - \left(\frac{\partial \mathbf{r}}{\partial \mathbf{T}} \right)^{-1} \frac{\partial \mathbf{r}}{\partial \mathbf{k}}, \quad (15)$$

$$\frac{d\mathbf{k}}{d\mathbf{c}} = \mathbf{A}. \quad (16)$$

Incorporating the earlier equations into the sensitivity Eq. 14, we derive the expression

$$\frac{dJ}{d\mathbf{c}} = \left(- \frac{\partial J}{\partial \mathbf{T}} \left(\frac{\partial \mathbf{r}}{\partial \mathbf{T}} \right)^{-1} \frac{\partial \mathbf{r}}{\partial \mathbf{k}} + \frac{\partial J}{\partial \mathbf{k}} \right) \mathbf{A}. \quad (17)$$

As a matter of fact, evaluating sensitivities requires the availability of the inverse of the stiffness matrix. However, this becomes costly for problems involving fine meshes. To mitigate this, the adjoint technique is commonly employed. This method involves initially computing the adjoint variables $\boldsymbol{\lambda}$, followed by the subsequent calculation of sensitivities

$$\boldsymbol{\lambda} = - \left(\frac{\partial \mathbf{r}}{d\mathbf{T}} \right)^{-T} \frac{\partial J}{\partial \mathbf{T}}, \quad (18)$$

$$\frac{dJ}{d\mathbf{c}} = \left(\boldsymbol{\lambda}^T \frac{\partial \mathbf{r}}{\partial \mathbf{k}} + \frac{\partial J}{\partial \mathbf{k}} \right) \mathbf{A}. \quad (19)$$

It should be noted that although adjoint-based sensitivity analysis avoids the explicit inversion and storage of the tangent matrix, it necessitates a linear solve for each objective and constraint function. Therefore, this approach may become prohibitively costly when multiple adjoint-based sensitivity analyses are required.

3. Finite operator learning

Building upon the concept of physics-informed neural networks Raissi et al. [12] and deep energy method Samaniego et al. [23], we construct a neural network based on the discretized weak form of the governing partial differential equations, as detailed in Section 2.1. The input layer consists of the design variables or parameters, while the output layer represents the unknown solution field, specifically nodal temperatures in this work. Additionally, constraints on the network's inputs and outputs - or any combination thereof - can be effectively enforced through a multi-objective loss function approach. This work is based on feed-forward neural networks. By denoting the information transfer from the $l - 1$ layer to l using the vector \mathbf{z}^l , each component of vector \mathbf{z}^l is computed by

$$z_m^l = a \left(\sum_{n=1}^{N_l} w_{mn}^l z_n^{l-1} + b_m^l \right), \quad l = 1, \dots, L. \quad (20)$$

In Eq. (20), z_n^{l-1} is the n -th neuron within the $l - 1$ -th layer. The component w_{mn} shows the connection weight between the n -th neuron of the layer $l - 1$ and the m -th neuron of the layer l . Every neuron in the l -th hidden layer owns a bias variable b_m^l . The number N_l corresponds to the number of neurons in the l -th hidden layer. The total number of hidden layers is L . The letter a stands for the activation function in each neuron. As a result, our feed-forward neural operator \mathcal{N} is mathematically expressed as

$$\mathbf{c} = [c_i], \quad \tilde{\mathbf{T}} = [\tilde{T}_j], \quad i = 1 \dots M, \quad j = 1 \dots N, \quad (21)$$

$$\tilde{\mathbf{T}} = \mathcal{N}(\mathbf{c}; \boldsymbol{\theta}), \quad \boldsymbol{\theta} = \{\mathbf{W}, \mathbf{b}\}. \quad (22)$$

Here, \mathbf{c} is the vector of M design parameters, $\tilde{\mathbf{T}}$ is the vector of N predicted nodal temperatures, and the trainable parameters of the network are denoted by $\boldsymbol{\theta}$. Fig. 4 schematically represents the proposed network for finite operator learning.

Next, we design the network's loss function to enforce the desired constraints on the inputs and outputs - or any combination thereof - in a multi-objective manner as

$$\mathcal{L}_{tot} = w_{ph} \mathcal{L}_{ph} + w_{bc} \mathcal{L}_{bc} + w_{se} \mathcal{L}_{se}. \quad (23)$$

Different terms in the above equation read as follows:

- $\mathcal{L}_{ph}(\mathbf{k}, \tilde{\mathbf{T}})$ ensures that the predicted nodal temperatures comply with the governing physical equations. This is achieved by minimizing either the energy functional or the sum of the nodal residuals

$$\mathcal{L}_{en}(\mathbf{k}, \tilde{\mathbf{T}}) = \sum_{e=1}^{n_{el}} \tilde{\mathbf{T}}_e^T \tilde{\mathbf{r}}_e, \text{ where } \tilde{\mathbf{r}}_e = \sum_{n=1}^{n_{int}} \mathbf{B}_e^T (\mathbf{N}_e^T \mathbf{k}_e) \mathbf{B}_e \tilde{\mathbf{T}}_e - \mathbf{f}_e, \quad (24)$$

$$\mathcal{L}_{re}(\mathbf{k}, \tilde{\mathbf{T}}) = \sum_{i=1}^{n_{no}} \tilde{r}_i^2, \text{ where } \tilde{r}_i = \sum_{e \in \Omega_i} \tilde{\mathbf{r}}_e. \quad (25)$$

Here, $\tilde{\mathbf{r}}$ denotes the nodal residuals computed from the predicted temperatures and Ω_i is the set of elements sharing node i . Note that the subscript e indicates that the corresponding variable is evaluated at the element level.

- $\mathcal{L}_{bc}(\tilde{\mathbf{T}})$ ensures compliance with non-Dirichlet boundary conditions, if applicable; if not, w_{bc} is set to zero. Dirichlet boundary conditions are automatically and strongly satisfied as the network predicts only the unknown nodal temperatures. In more complex conditions, where the Dirichlet BCs change during simulation or in case the user wants to apply the Dirichlet BCs in a soft manner, then the following term can easily be added to $\mathcal{L}_{bc} = w_{db} \sum_{i=1}^{n_{db}} (T_i - T_{i,db})^2$.
- $\mathcal{L}_{se}(\mathbf{c}, \tilde{\mathbf{T}})$ ensures that the network's output-to-input sensitivity, denoted by $d\tilde{\mathbf{T}}/d\mathbf{c}$, complies with the requirement that the residuals must be stationary with respect to the design variables, as outlined in Eq. 15. Specifically, the equation governing this condition is

$$\begin{aligned} \frac{d\tilde{\mathbf{r}}}{d\mathbf{c}} &= \frac{\partial \tilde{\mathbf{r}}}{\partial \tilde{\mathbf{T}}} \frac{d\tilde{\mathbf{T}}}{d\mathbf{c}} + \frac{\partial \tilde{\mathbf{r}}}{\partial \mathbf{k}} \frac{d\mathbf{k}}{d\mathbf{c}} \\ &= \mathbf{K} \frac{d\tilde{\mathbf{T}}}{d\mathbf{c}} + \frac{\partial \tilde{\mathbf{r}}}{\partial \mathbf{k}} \mathbf{A} \\ &= \mathbf{0}. \end{aligned} \quad (26)$$

where \mathbf{K} is the tangent stiffness matrix of FEM, \mathbf{A} is the tangent matrix of the parameterization, and $\partial \tilde{\mathbf{r}} / \partial \mathbf{k}$ is the tangent matrix of FEM w.r.t the physical design field and it can be analytically calculated. By aggregating the violations of the specified stationary condition across all nodes, the corresponding loss function is defined as

$$\mathcal{L}_{se}(\mathbf{c}, \tilde{\mathbf{T}}) = \sum_{i=1}^{n_{nodes}} \sum_{j=1}^{n_c} \left(\frac{d\tilde{r}_i}{dc_j} \right)^2. \quad (27)$$

It should be noted that by incorporating these target derivatives into the total loss function, we essentially engage in what is known as Sobolev training [63]. This approach not only ensures the correct output-to-input sensitivity of the network but also results in surrogate models that deliver higher accuracy in predicted values.

Finally, the total loss term is minimized concerning the trainable parameters to find the optimal trainable parameters $\boldsymbol{\theta}^*$ via a desired optimizer

$$\boldsymbol{\theta}^* = \arg \min_{\boldsymbol{\theta}} \mathcal{L}_{tot}(\mathbf{c}, \boldsymbol{\theta}, \tilde{\mathbf{T}}). \quad (28)$$

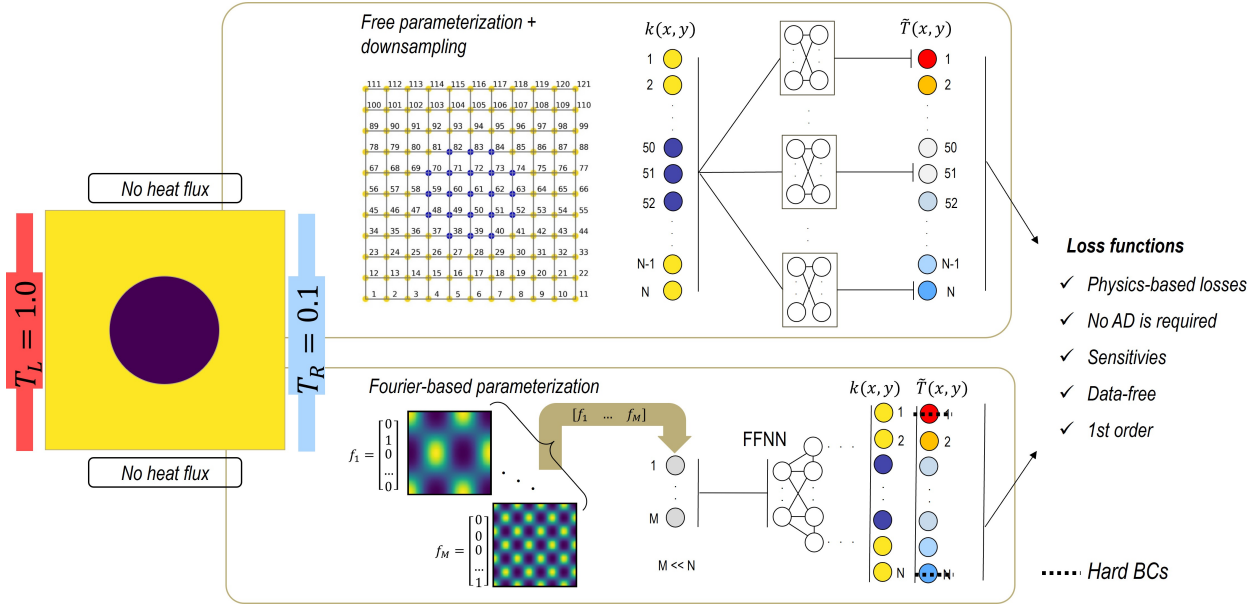


Figure 4: Network architecture for finite operator learning, where information about the input parameter at each grid point goes in and the unknown is evaluated utilizing a series of separate deep neural networks.

Remark 1 As described in Fig. 4, one can also utilize separate neural networks for predicting nodal unknowns (i.e., temperature values). Nevertheless, even with a standard fully connected neural network, one can set up the FOL framework for further computations.

Remark 2 In Eq. 23, there is no involvement of automatic differentiation, and all the derivatives are approximated using the shape functions from the finite element method. In simpler terms, the loss function in this work is an algebraic equation.

Remark 3 The proposed FOL framework has several flexibilities that make it suitable for various applications. First, although the method is data-free, data can certainly be combined with available physics, similar to the original PINNs and other neural operators. Second, one can easily represent the input layer based on other desired parameter spaces (e.g., fiber-reinforced composites or Voronoi tessellation-based parameterization for polycrystalline materials). Third, while the ideas presented here are mainly based on FEM, the concept can be extended to other numerical frameworks such as finite difference, finite volume, spectral solvers, and even non-local interaction-based equations such as peridynamics. Note that in the extreme case, where we provide the NN with only one sample (i.e., one set of parametric input), the method reduces to a classical FE-adjoint solver.

Remark 4 In the current framework, we expect three different convergence studies. First, we need to train with a sufficient number of epochs. Second, we need to ensure the mesh resolution is adequate for the output layer. Third, for parametric learning, we need to ensure that a sufficient number of (random) samples is provided for the FOL.

4. Results

This section is divided into three main parts. First, we briefly discuss the generation of collocation fields for the data-free training process. Next, we present the results of parametric learning of the governing equations described in Eq. 3. This includes a comprehensive study on the accuracy of FOL-based predictions for both the primal field and sensitivities. Lastly, we demonstrate gradient-based optimization using a pretrain-free FOL approach, where the learning process is nested within each design iteration and the gained knowledge is transferred to the next iteration. This is the so-called NAND optimization using FOL for primal and sensitivity analysis.

In all the 2D results provided in this section, we focus on the geometry and boundary conditions described in the left-hand side of Fig. 4 unless mentioned otherwise. Moreover, for the sake of simplicity, the mesh and domain of interest remain structured and square-shaped. Furthermore, for the sensitivity study and optimization, heat transfer in the y-direction is considered as the objective, while heat transfer in the x-direction is treated as the constraint. These functions are mathematically expressed as

$$J = \int_{\Omega} (-k \nabla_y T)^2 dV, \quad (29)$$

$$h = \int_{\Omega} (-k \nabla_x T)^2 dV - 0.125, \quad (30)$$

where J and h are the objective and constraint functions, respectively. For the full optimization problem definition, please refer to Section 2.3. Finally, we would like to mention that extending the presented frame and studies to unstructured meshes or arbitrarily shaped geometries is straightforward. For the sake of brevity, these extensions are not fully discussed here. For such studies, please refer to [72, 73]. It is noteworthy that the training can be conducted on personal laptops without GPU acceleration, owing to the efficiency of the proposed framework. However, we primarily utilized a Quadro RTX 6000 GPU unless stated otherwise.

4.1. Sample preparation

We have discussed two sets of parametrization approaches in this work. Regardless of the user’s choice, each parametrization approach requires exploring the possible options in the parametric space. By providing the network with a sufficiently diverse set of inputs, the performance of the deep learning model will improve. Here, we will briefly discuss our strategies to explore each design space.

4.1.1. Free parameter design

It is noteworthy that even for a selected reduced grid (with 11×11 nodes) and considering a two-phase material, there can be $2^{121} \approx 2.6 \times 10^{36}$ independent samples which is almost unfeasible to cover. Hence, the user should determine the relevant parameter space specific to each problem. Based on the description in Section 2.2.1, we generate 4000 samples. A subset of the generated samples is presented in Fig. 5. Additionally, some samples are chosen for testing (see Fig. 6). These test cases are entirely novel and some are deliberately selected for their symmetrical aspects, ensuring they are beyond the scope of the training dataset. The corresponding histograms for volume fraction and dispersion value are depicted in Fig. 7.

A summary of the network’s (hyper)parameters is presented in Table 1. Note that whenever multiple options for a parameter are introduced, we examine the influence of each parameter on the results.

Table 1: Summary of the network parameters.

Parameter	Value
Inputs, Outputs	$\{k_i\}, \{T_i\}$
Activation function	tanh, swish, sigmoid, linear
Number of layers and neurons for each sub-network (L, N_l)	(2, 10)
Optimizer	Adam
Number of initial samples	2000, 4000
Batch size	50, 100
(Learning rate α , number of epochs)	(10^{-3} , 5000)

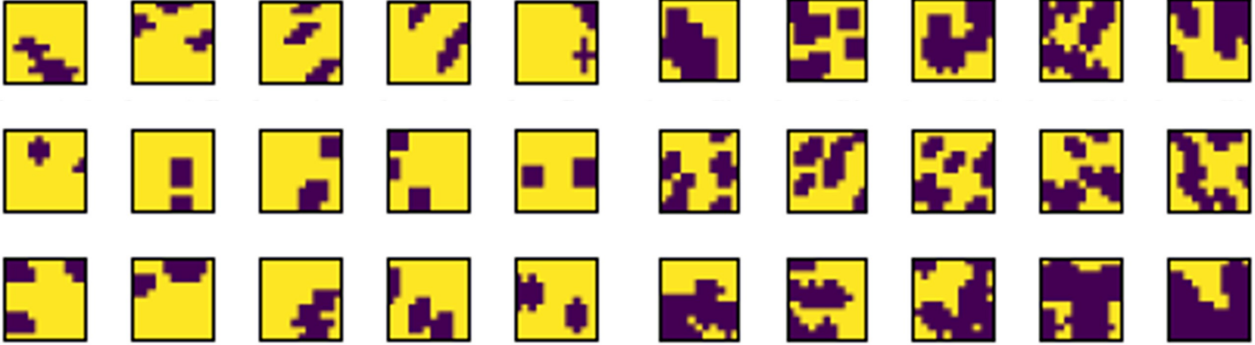


Figure 5: Examples showcasing created morphologies for a two-phase microstructure.

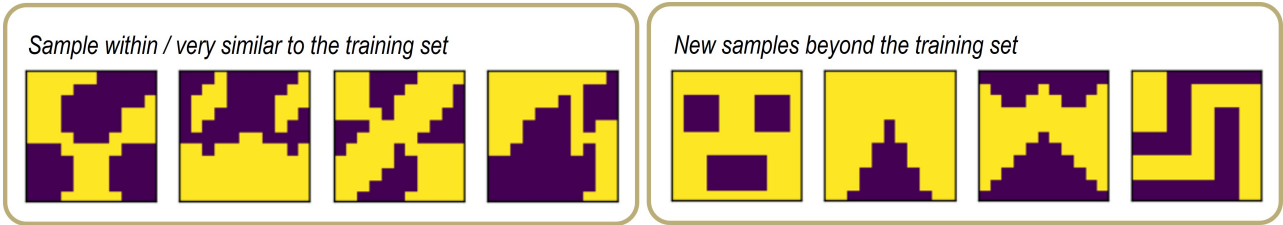


Figure 6: Unseen samples used for testing the neural network after training.

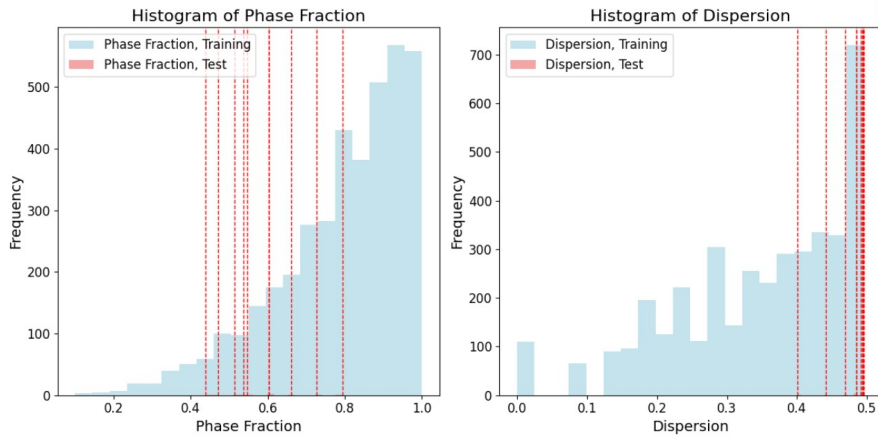


Figure 7: Histogram of the phase fraction as well as dispersion values of the created samples.

4.1.2. Fourier-based parametrization

We now turn into Eq. 10. For the rest of the study, and for simplification purposes, only the constant term as well as the last term involving the multiplication of two cosine functions are considered (i.e., $A_i = 0$, $B_i = 0$, $C_i = 0$). However, even by limiting ourselves to these terms, one can produce many designs for the property function k_f . We select three frequencies for each direction. Considering the constant term, this choice gives us $M = 3 \times 3 + 1 = 10$ different terms, which can be added up to construct $k(x, y)$ according to Eq. 11 and Eq. 10. See also Table 2 for a summary of the Fourier-based parameterization for the FOL model.

Table 2: Parameters used for generating conductivity samples in training the Fourier-based FOL.

Parameter	Value
Inputs, Outputs	$\{\text{freq}_i\}, \{T_i\}$
Frequency in the x - direction $f_{x,i}$	$\{3, 5, 7\}$
Frequency in the y - direction $f_{y,i}$	$\{2, 4, 7\}$
Number of random samples	8000
Neurons in the input layer (input features, freq_i)	10
Mesh (Neurons in the output layer without DBCs)	51×51 (5202)
Act. func., hidden layers, learning rate, Epoch num.	Swish, [300, 300], 0.001, 1000

The input samples used for training are generated by combining different random distributions for these ten inputs. A summary of all the 8000 selected samples is shown in Fig. 8. See Fig. 9 for a few examples of samples obtained by the Fourier-based parameterization.

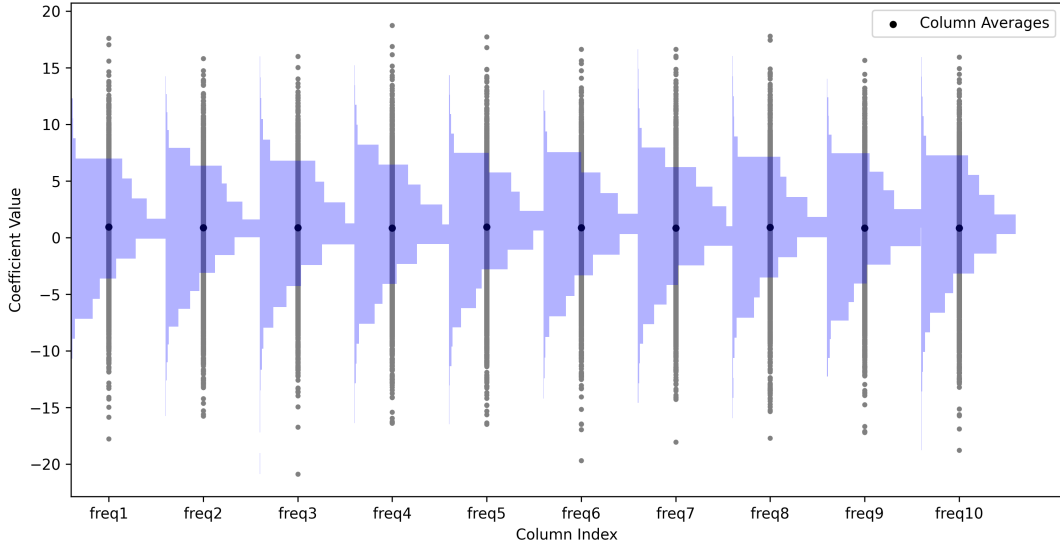


Figure 8: Distribution of the 8000 random values for components of each frequency term. The parameter freq_i represents the i -th coefficient corresponding to the i -th frequency.

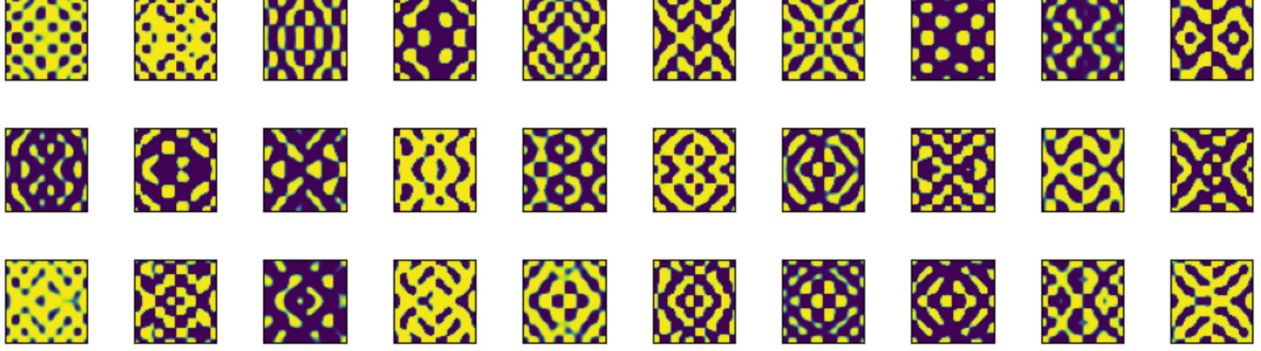


Figure 9: Examples showcasing created morphologies for a two-phase microstructure.

A few unseen test cases are also selected for checking the performance of the trained network beyond the training set. In some test cases, the matrix material is highly conductive, while in others, the matrix acts as an insulating material with highly conductive inclusions. The distribution of these frequencies is randomly generated and deliberately selected to be uncommon in the training set (i.e., $5 < \text{freq}_i < 10$). This allows us to test the performance of the pre-trained parametric FOL. For a given image of the microstructure, using the Fourier-based parameterization, one must first perform an inverse Fourier analysis to find the corresponding coefficients. See Table 3 for the chosen amplitudes of the test cases and Fig. 10 for the corresponding conductivity maps.

Table 3: Selected test cases and corresponding Fourier coefficients.

Study type	Value ($\text{freq}_i, i = 1 \dots 10$)
Microstructure 1 (Figs. 14a 14b 14c)	[5.3, 6.0, 7.7, 5.1, 5.1, 6.8, 5.5, 8.3, 8.1, 7.5]
Microstructure 2 (Fig. 15)	[0.7, -0.5, -0.0, 0.3, 0.9, 1.6, -0.2, 0.9, -0.3, -1.3]
Microstructure 3 (Fig. 16)	[-1.7, 0.7, -0.8, 0.6, 0.3, 0.5, -0.8, -0.9, 1.8, -0.6]
Microstructure 4 (Fig. 17)	[-3.6, 0.8, 0.5, 2.0, 3.8, 0.0, -0.8, 2.6, 0.3, -0.3]

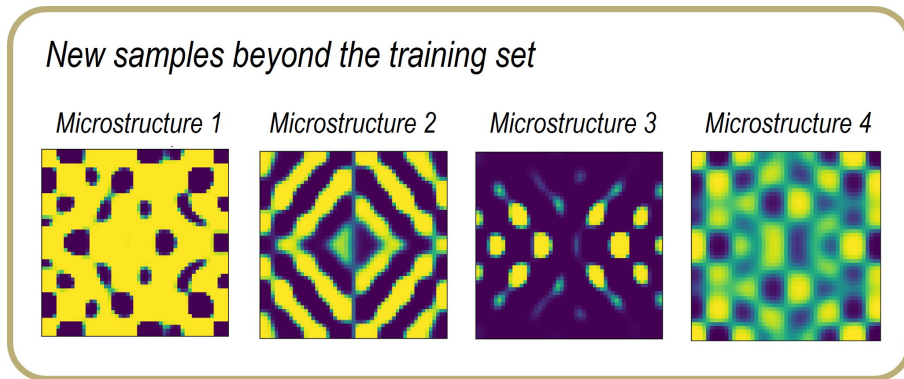


Figure 10: Unseen samples used for testing the neural network after training.

4.2. Parametric learning and sensitivity analysis

The algorithms developed in this study are implemented using JAX [74] software. The codes are also implemented in the SciANN package [75], and the methodology can be adapted to other programming platforms as well. The material parameters listed in Table 4 are selected to maintain the temperature values within the range of 0 to 1. However, alternative parameters and boundary values can be chosen, and the model variables can be normalized to ensure they fall within the range of -1 to 1 .

Table 4: Model input parameters for the thermal problem.

	heat conductivity value / unit
Phase 1 (k_{mat})	1.0 W/mK
Phase 2 (k_{inc})	0.01 W/mK
Applied temperature (T_L, T_R)	(1.0 K, 0.0 K) or (1.0 K, 0.1 K)

In the first set of studies, the Dirichlet boundary conditions are satisfied in a soft manner via a penalty term to demonstrate the framework’s flexibility in handling such cases. As will be explained later, these terms can easily be imposed in a hard manner as well. Furthermore, the loss term related to sensitivities is switched off at first to evaluate the performance of the network solely based on the discretized energy form of the problem. For the loss term related to Dirichlet boundary conditions, we assigned higher weightings to expedite the satisfaction of the boundary terms. Following a systematic study that began with equal weightings for both loss terms, we selected $w_{db} = 10$.

In Figures 11 and B.24, the predictions of the same neural network for various sample test morphologies (i.e., conductivity maps) are depicted across different numbers of epochs, presented in separate columns. The last column displays the reference solutions obtained by the finite element method, utilizing the same number of elements (10 by 10 elements or 11 by 11 nodes). It is important to note that post-training, the results are assessed on finer grid points (165×165) using simple shape function interpolations, which lend a smoother appearance to the results. For conciseness, all temperature values are denoted in Kelvin [K], heat flux is represented in [W/m^2], and thermal conductivity is expressed in [W/mK].

As depicted in Fig. 11, the NN’s outcomes are unreliable before 1000 epochs. Surprisingly, only after 1000 epochs, the NN demonstrates an acceptable level of training. Training further resulted in some improvements, which are particularly noticeable in sharp discontinuities near the phase boundaries. It is noteworthy that the results showcased in Figures 11 and B.24 correspond to test cases, where these morphologies are unseen by the NN. More comprehensive comparisons and quantitative error analyses are provided in subsequent sections.

Remark 5 Rather than relying on finite element interpolation functions, which do not add any additional information and merely smooth the results, an alternative approach involves employing a pre-trained decoder network. This network can map the solution space from a coarse grid to a finer grid. Similar ideas have been explored in [38].

Remark 6 We exclusively predict temperature profiles in the current approach. Consequently, the flux vector, as presented in subsequent studies, is derived via local numerical differentiation of the temperature. However, an extension of this approach could involve a mixed formulation, predicting the flux values as additional outputs for the network to further enhance predictions, as explored in works such as [3, 11, 28].

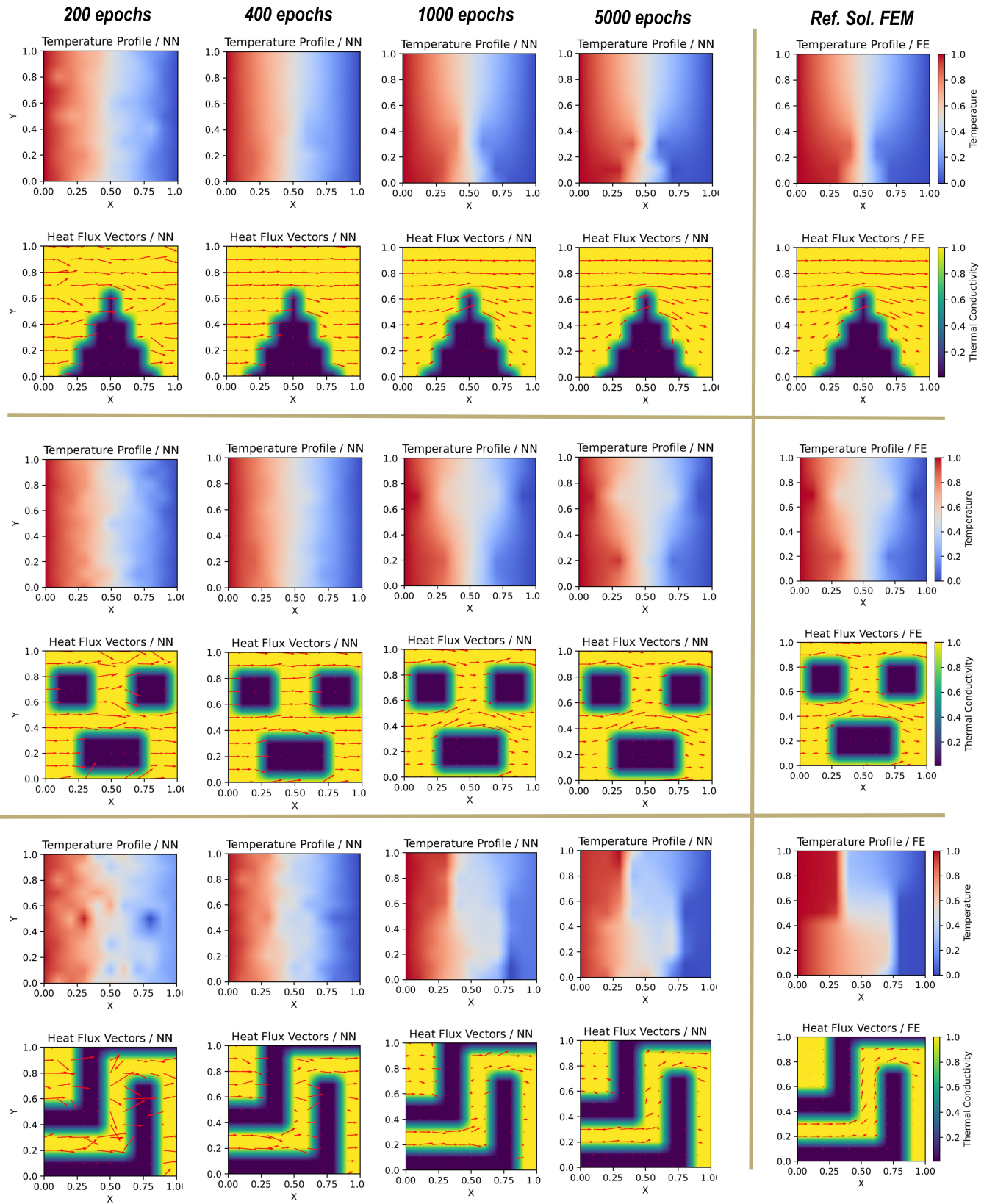


Figure 11: Predictions of the trained FOL for different numbers of epochs.

4.2.1. Comparison of physics-driven and data-driven deep learning models

In this part, we seek to demonstrate the implications of using traditional numerical models, gathering their data, and training a neural network in a supervised manner. This latter approach, termed data-driven, is widely pursued by many researchers. To conduct this comparison, we utilize the same set of 4000 sample data, perform finite element calculations for each, and store the associated solutions. We employ an identical network architecture to train the data-driven network. The comparison results are illustrated in Fig. 12 for a specific test case. For an unseen test case, the physics-driven method provides more accurate predictions for temperature and flux distribution. The error in this study is based on $Err = \frac{\sqrt{\sum_i (T_{NN}(i) - T_{FE}(i))^2}}{\sqrt{\sum_i (T_{FE}(i))^2}} \times 100$.

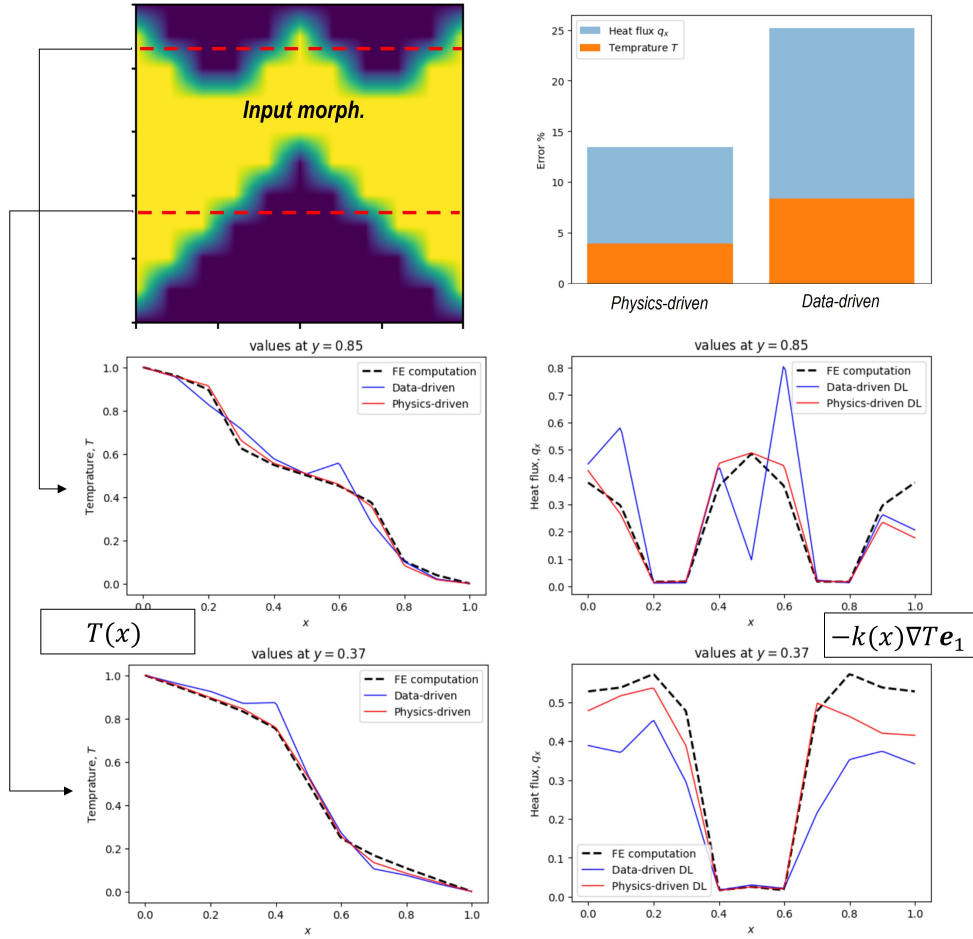


Figure 12: Comparison of data-driven and physics-driven approaches regarding the temperature and flux profiles.

The observations and conclusions mentioned above are not confined to the test case. This significantly underscores the appeal of the physics-driven model for two primary reasons: 1) It does not rely on labeled data for training, and 2) it delivers more accurate predictions for unseen cases. However, we should report that the supervised training requires a lower training cost (approximately 10 times less, on average) than the physics-based approach. Moreover, it is challenging, if not impossible, to assert that there is no potentially better NN for improving the data-driven approach. Therefore, further investigations using other types of architectures for physics-driven and data-driven neural networks are important for future studies.

4.2.2. Influence of the number of training samples

In Fig. 13, we analyze the impact of the number of initial sample fields. In the selected 2000 samples, we excluded mainly morphologies with ring shape. For the depicted test cases, we observed a reduction in the maximum difference by a factor of 2.0 and 1.6. This suggests that enhancing the quantity and diversity of initial random fields can improve the quality of results for unseen test cases. The training cost did not increase as we doubled the batch size while increasing the number of samples.

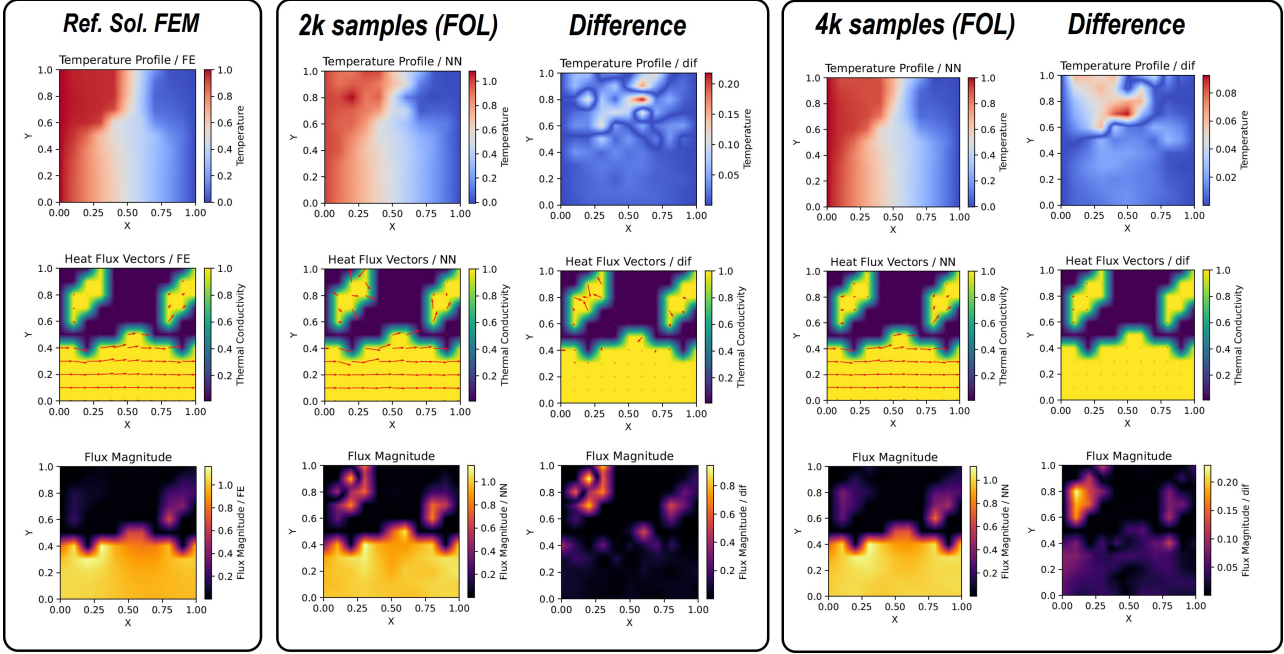


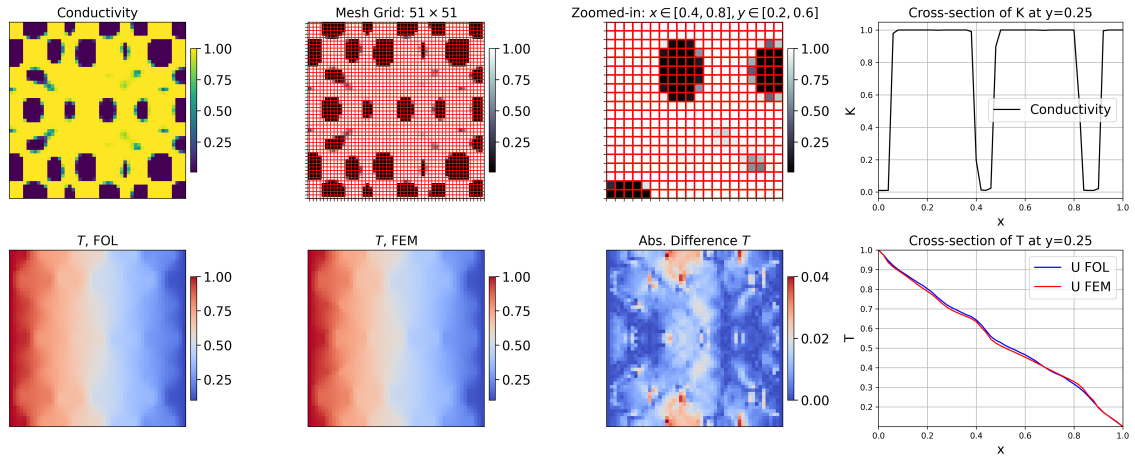
Figure 13: Influence of the initial training fields for the introduced physics-informed deep learning model (FOL).

4.2.3. Fourier-based parameterization for FOL: Mesh and sample convergence

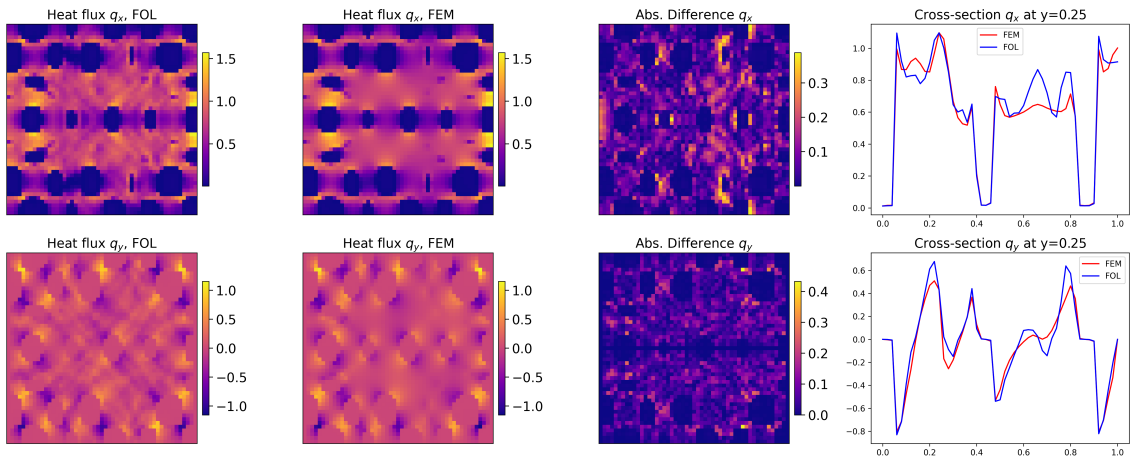
We now switch to the second formulation for the FOL framework, which is primarily based on a reduced set of input parameters using Fourier analysis (see also Fig. 4). Moreover, we take advantage of applying hard boundary constraints. We use $T_R = 0.1$ K and $T_L = 1.0$ K to show the flexibility of the method to handle other BCs. Note that for the rest of the paper, all the loss terms defined in Eq. 23 are now active unless it is mentioned otherwise for further studies.

The results reported in Figs. 14a, 14b, and 14c, show an acceptable agreement between the two methods for forward temperature profile, obtained heat fluxes and sensitivities, respectively. All these results are obtained for the 51×51 and no interpolation or any other additional post-processing step is done. Again, we noticed that the results for the spatial derivatives of the temperature field show more fluctuations as the network is solely trained to obtain the temperature field. Nevertheless, the errors for the heat flux components q_x and q_y seem to be acceptable, especially when considering the averaged values (see also the results in Fig. 12 and relative quantitative comparisons).

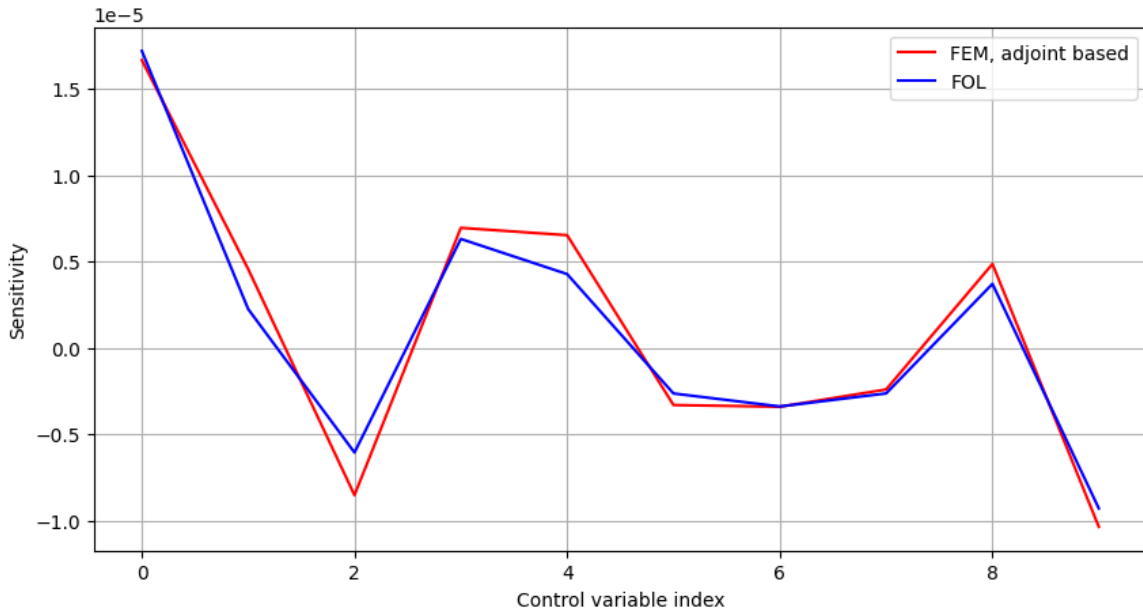
In Figs. 15 and 16 further unseen test cases are shown for the temperature predictions. Note that in these selected samples, we have extreme conditions of isolation within the microstructure, and therefore, a very sharp solution is expected and observed for the temperature field. Despite the challenging nature of these two test cases, the predictions of the FOL after just one training session seem to agree well with FEM.



(a) Comparison of the temperature profile between FOL and FEM.



(b) Comparison of heat flux profiles between FOL and FEM.



(c) Comparison of FOL-based and FEM-based sensitivities for the given microstructure.

Figure 14: Results of pre-trained FOL for a random unseen microstructure using [5.3, 6.0, 7.7, 5.1, 5.1, 6.8, 5.5, 8.3, 8.1, 7.5].

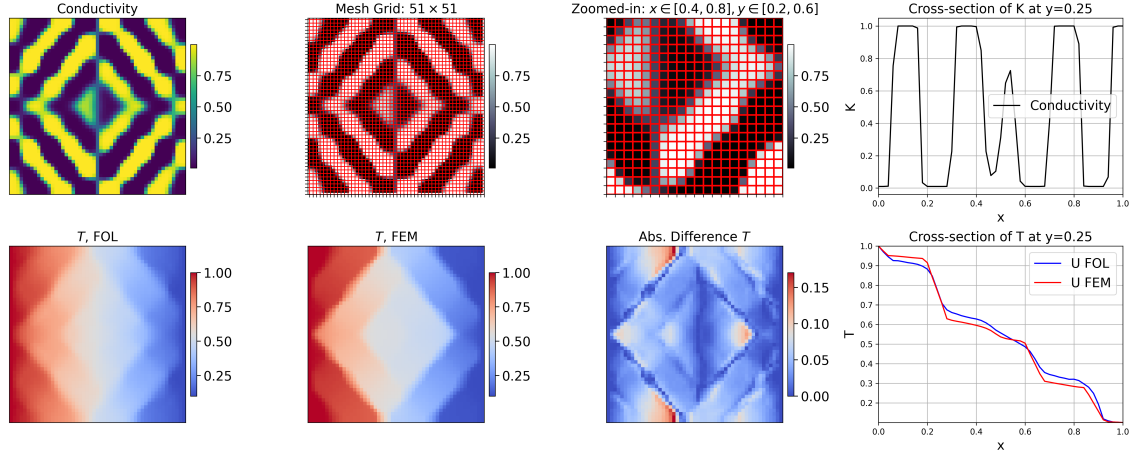


Figure 15: Comparison of the deformation profile between FOL and FEM for a random microstructure using $[0.7, -0.5, -0.0, 0.3, 0.9, 1.6, -0.2, 0.9, -0.3, -1.3]$.

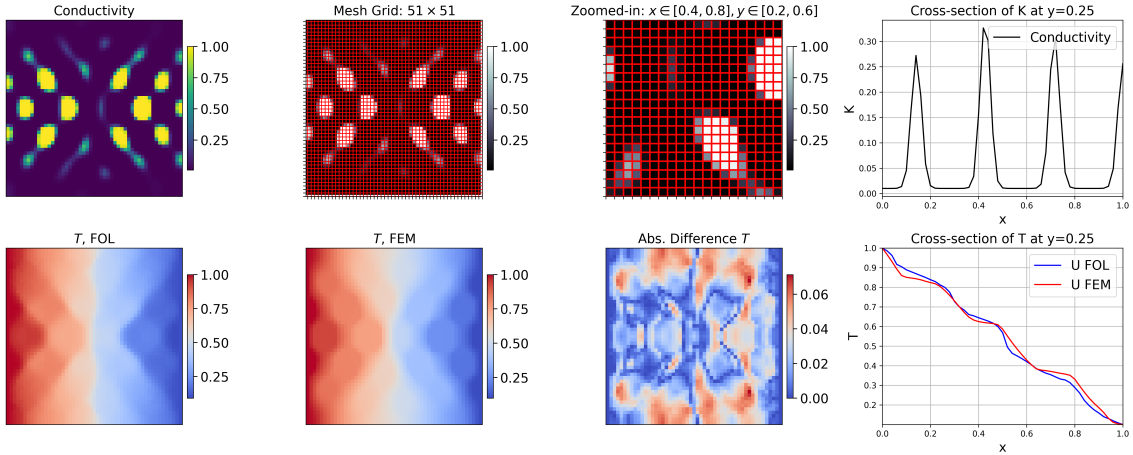


Figure 16: Comparison of the deformation profile between FOL and FEM for a random microstructure using $[-1.7, 0.7, -0.8, 0.6, 0.3, 0.5, -0.8, -0.9, 1.8, -0.6]$.

Next, we check for mesh convergence with different choices of N as shown in Fig. 17. To ensure a fair comparison, we train the same network described in Table 2 with just a different number of neurons in the output layer, which is directly determined based on the mesh resolution. Interestingly, the training and evaluation times (or costs) remain almost unchanged. Moreover, we observe a significant reduction in evaluation cost compared to the FEM as we go to higher mesh densities. See also the results provided in Fig. 18 for the normalized training and evaluation costs. We confirm a clear convergence for the temperature profile using denser meshes. For brevity, we recorded the following temperature values for the mesh densities shown in Fig. 17 at point $x_P = 0.6$ and $y_P = 0.25$, we have $T_P^{11 \times 11} = 0.455$, $T_P^{21 \times 21} = 0.460$, and $T_P^{51 \times 51} = 0.461$. Generally, the higher the frequency and phase contrast, the greater the number of elements needed. For the current work and chosen parameters, a mesh of 50×50 was sufficient according to our studies.

Finally, we investigate the influence of the additional sensitivity loss or the Sobolev training on the prediction accuracy of the trained network for a set of unseen test cases. To gain better insight, we also varied the number of initial sample fields for each comparison. In Fig. 19 we

show the error reduction by increasing the number of samples for training. Furthermore, by adding the sensitivity loss term into the training, we managed to further reduce the average error observed in the test cases.

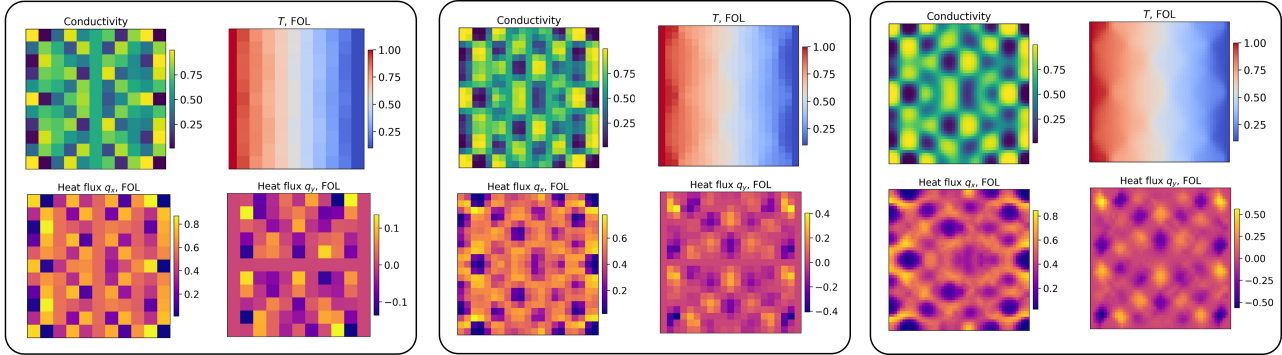


Figure 17: Mesh convergence analysis for a random microstructure using $[-3.6, 0.8, 0.5, 2.0, 3.8, 0.0, -0.8, 2.6, 0.3, -0.3]$.

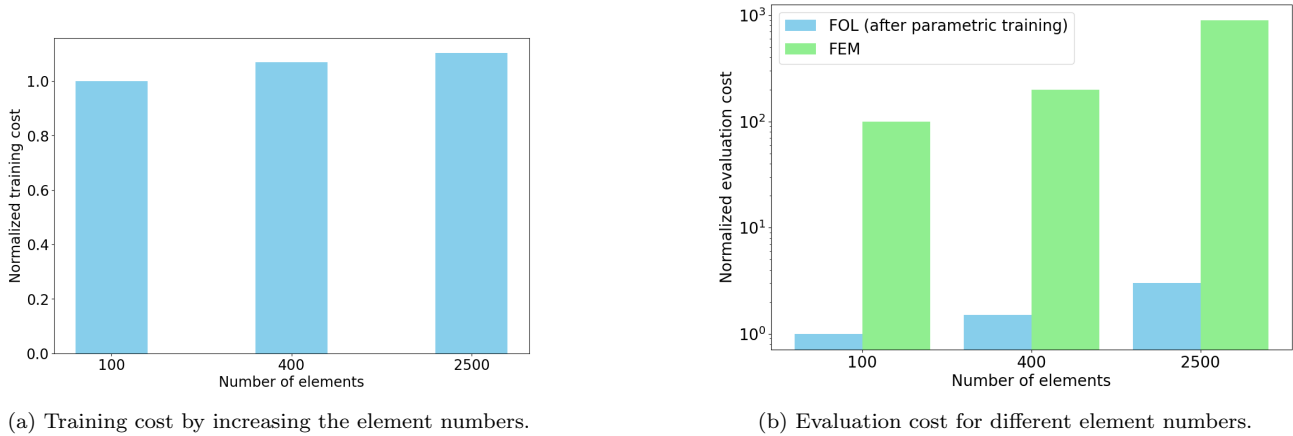


Figure 18: Comparison of the training and evaluation costs for FOL and FEM.

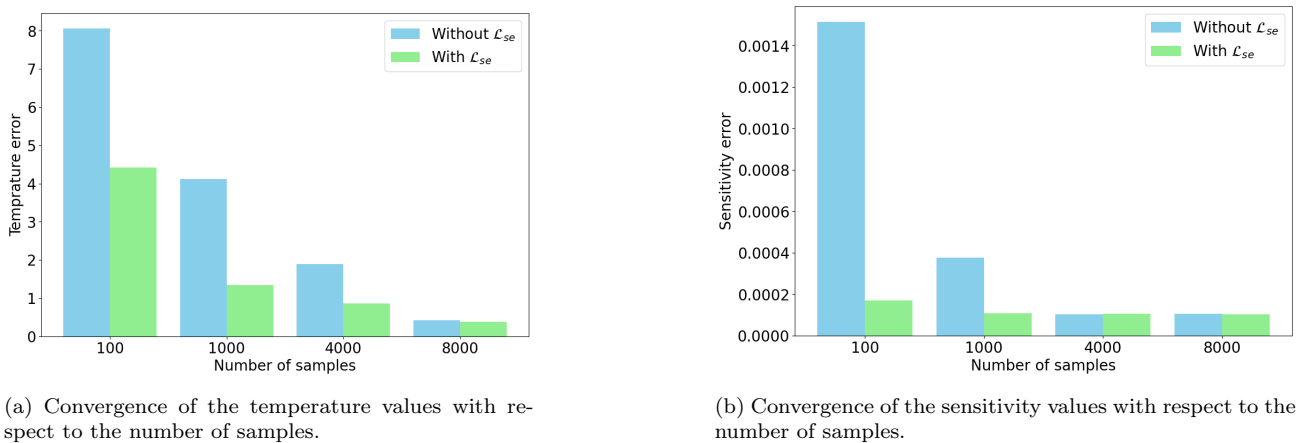


Figure 19: Error analysis for the physics-informed parametric learning. The Sobolev training, or adding an additional loss for sensitivities, significantly improved the average errors in the test cases for both the forward prediction of the temperature field and the sensitivity values.

4.3. Optimization

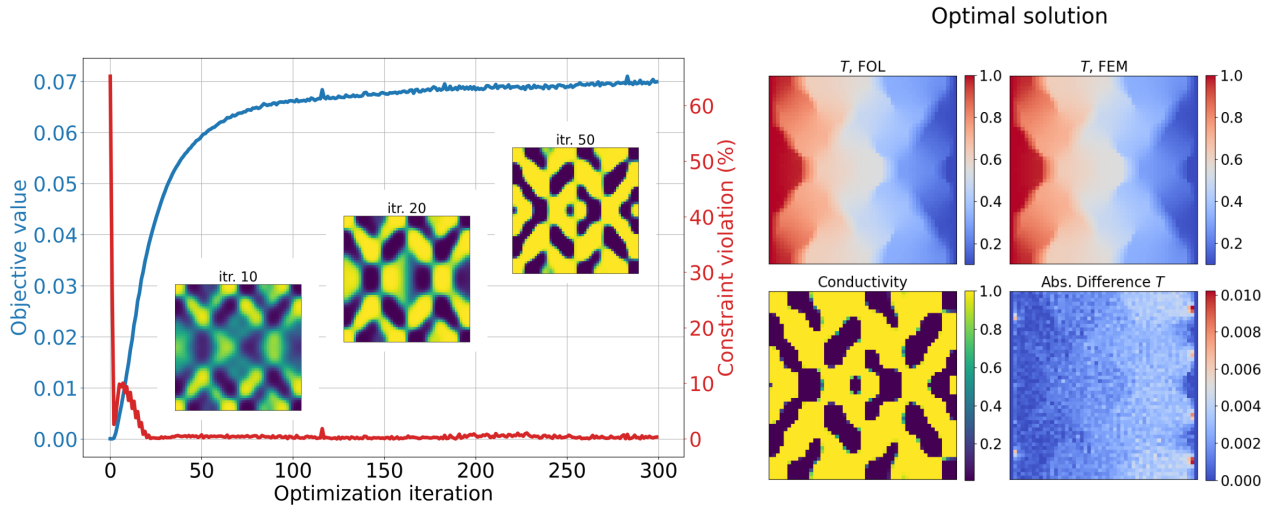
Encouraged by the strong performance of FOL in forward and sensitivity analysis, we test the methodology to perform gradient-based optimization. As previously discussed in the introduction of this section, our objective is to enhance heat transfer capabilities in the y -direction while constraining it in the x -direction. For this purpose, based on the mesh study results, a mesh resolution of 51×51 is chosen, see Fig. 17. Furthermore, we employ Fourier parametrization with frequencies in x - direction $\{5, 7, 9\}$ and in y - direction $\{4, 6, 8\}$. Starting from a uniform conductivity field of 0.5, with Fourier’s weights set to zero except for the first, gradient-based optimization is performed iteratively until there is no significant change in the objective value. A hyperparameter study was conducted on the network’s structure to determine the optimal number of layers and neurons. Relative errors in constraint values and gradients for different network architectures, both with and without considering the sensitivity loss, are reported in Table 5. These results underscore the importance of the sensitivity loss function in ensuring accurate solution-to-design sensitivities. The selected architecture for the FOL-based results in this Section is highlighted in Table 5. This architecture strikes a good balance between the network’s density and its accuracy in both values and sensitivities.

Table 5: Errors (%) in constraint values and gradients for different network architectures, both with and without considering the sensitivity loss. FEM-based values and adjoint-FEM-based gradients are used as references for error calculation. $N = 51$. The case used for optimization is highlighted in red.

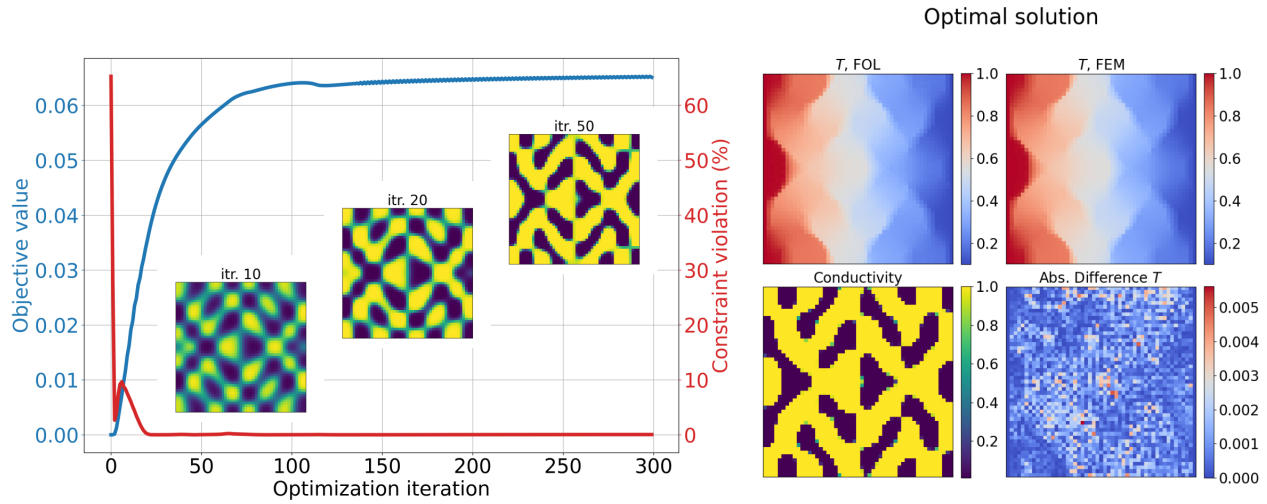
Layers	$w_{se} = 1$	$w_{se} = 0$	Layers	$w_{se} = 1$	$w_{se} = 0$	Layers	$w_{se} = 1$	$w_{se} = 0$
[$N/3$]	(0.96,12.39)	(1.20,218.75)	[$N/3,N/3$]	(2.06,20.35)	(0.19,217.73)	[$N/3,N/3,N/3$]	(2.11,24.43)	(0.84,229.57)
[N]	(1.61,8.39)	(1.82,239.37)	[N,N]	(2.59,8.84)	(0.99,180.90)	[N,N,N]	(1.60,16.08)	(0.56,218.10)
[10 N]	(1.42,9.65)	(0.56,358.86)	[10 $N,10N$]	(3.64,6.77)	(1.41,590.13)	[10 $N,10N,10N$]	(0.91,6.76)	(1.44,167.49)
[25 N]	(3.40,10.58)	(2.47,1019.49)	[25 $N,25N$]	(3.63,7.08)	(1.59,252.81)	[25 $N,25N,25N$]	(4.47,5.69)	(1.96,136.96)

The results of maximizing J (Eq. 29) while constraining h (Eq. 30) to 0.0 are shown in Fig. 20. Two cases are considered: a) FOL-driven optimization, where the primal and sensitivity analyses are conducted simultaneously by minimizing the FOL’s total loss function (Eq. 23) at each optimization iteration, and b) FEM-driven optimization, where the primal and sensitivity analyses are performed sequentially using FEM and adjoint FEM, respectively. While both optimal solutions satisfy the constraint, the FOL-driven optimization achieves approximately 7.5% more improvement in the objective function. This additional improvement accounts for the differences observed in the optimal conductivity and temperature fields.

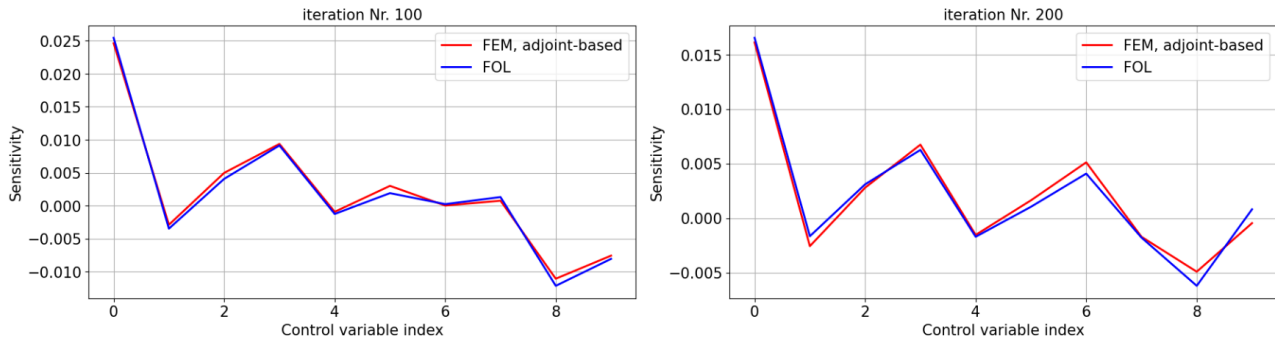
When comparing the convergence histories in Figs. 20a, 20b, fluctuations are observed in the FOL-driven optimization, which may be attributed to possible errors in the temperature field, sensitivities, or both. Motivated by this observation, in Fig. 20c, we compare the FOL-based and adjoint-based sensitivities of the constraint function h at certain optimization iterations. Both quantitatively and qualitatively, the results are in very close agreement. The minor deviations can be attributed to local errors in the FOL-based temperature field compared to the reference. These local errors directly lead to discrepancies in the sensitivities. Furthermore, the observed fluctuations can be attributed to the fixed number of training epochs and may also indicate the challenge of balancing loss functions and tuning the network’s hyperparameters.



(a) FOL-driven optimization: temperature and sensitivity fields are obtained by training FOL's neural network at each optimization iteration, without any perturbing.



(b) FEM-driven optimization: temperature and sensitivity fields are calculated using FEM and adjoint-FEM, respectively.



(c) Comparison of FOL-based and FEM-based sensitivities at selected iterations of the FOL-driven optimization.

Figure 20: Results of gradient-based optimization using Fourier parametrization with $f_x = \{5, 7, 9\}$, $f_y = \{4, 6, 8\}$.

Finally, we compare the computational performance of the FOL-driven and FEM-driven optimizations, as shown in Fig. 21. It should be noted that both FOL and FEM implementations utilize the JAX framework in Python. While the traditional FEM is implemented by computing

element stiffness matrices and assembling them into the global matrix, AD-based FEM leverages automatic differentiation to derive the residuals and stiffness matrix. The first observation is that FOL-based optimization outperforms traditional FEM and AD-FEM by factors of 27.09 and 1.2, respectively. However, it should also be mentioned that the linear solves in FEM computations are performed using the solve function from the linear algebra library of JAX. Another important point to consider is that the computational cost of FOL-based sensitivity analysis is completely independent of the number of response functions, whereas the cost of FEM-based sensitivity analysis scales directly with it.

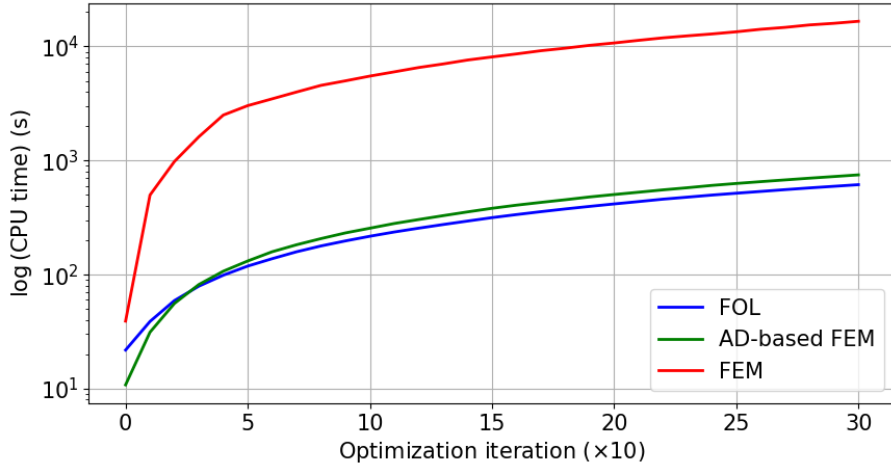


Figure 21: History of the total computational time for FOL-driven and FEM-driven optimizations. AD-based FEM computes residual and stiffness matrices using the automatic differentiation capabilities of JAX.

4.4. FOL as matrix-free PDE solver

The presented framework integrates machine learning techniques with numerical PDE solvers, such as FEM, to solve for discrete unknowns. As discussed in the previous section, when the batch size is set to one and only one sample is provided for training, the proposed methodology reproduces FEM-based results. However, unlike Newton-based solvers, FOL eliminates the need to construct and invert the tangent matrix of the underlying discretized PDE. Instead, the tangent matrix of the neural network is used to iteratively update the predicted solution during the backward propagation process. This occurs without explicitly constructing the matrix, which has two main advantages. First, the required memory is significantly reduced, especially when we are dealing with many nodes (or degrees of freedom). Second, we accelerate the solving process compared to similar FEM methods based on automatic differentiation.

The question arises about how accurate and fast the new solver is. Answering all the details and making a fair comparison between FOL and other numerical methods is a tedious task since many factors, from hardware to software platforms, play a role. Nevertheless, we intend to open up the discussion on this matter with the following example. To demonstrate the performance of the method in this context, we examine a nonlinear version of the heat equation where the heat conductivity coefficient is assumed to be temperature-dependent according to

$$k(T) = k_0 + \beta T^c. \quad (31)$$

Here, $\beta = 2$ and $c = 4$ are selected and the above term is inserted in Eq. 3. Our motivation is mainly for academic study, and we are not investigating any particular physical system and more investigations with greater nonlinearity should be conducted in future studies.

Utilizing the FOL method, one can easily define and link the finite number of output sensor points via an unstructured mesh. Utilizing unstructured meshes is suitable for discretizing complex geometries. To demonstrate this capability, in the following example, we perform the analysis on a complex geometry shown in Fig. 22. In this example, the far left and right surfaces are subjected to Dirichlet boundary conditions with fixed temperatures of 1.0 and 0.1, respectively. All other surfaces, including the curved and straight ones, are flux-free or isolated. The domain of interest is also heterogeneous, with the initial conductivity field varying spatially as shown in Fig. 22. The performance of the matrix-free solver FOL is extraordinary, showing a maximum pointwise error of 0.4 %.

For the chosen mesh, we again have 10 inputs representing the contributions of different frequency numbers, exactly as before. However, we now have 5485 neurons in the output layer, which represent all the degrees of freedom (i.e., discretized solution space). For this training, we used only one layer with one neuron since we are not interested in the parametric solution or sensitivities. This choice is sufficient to solve all the unknowns. Furthermore, the system is trained for approximately 1000 epochs with a learning rate of 0.001. The activation function is the swish function.

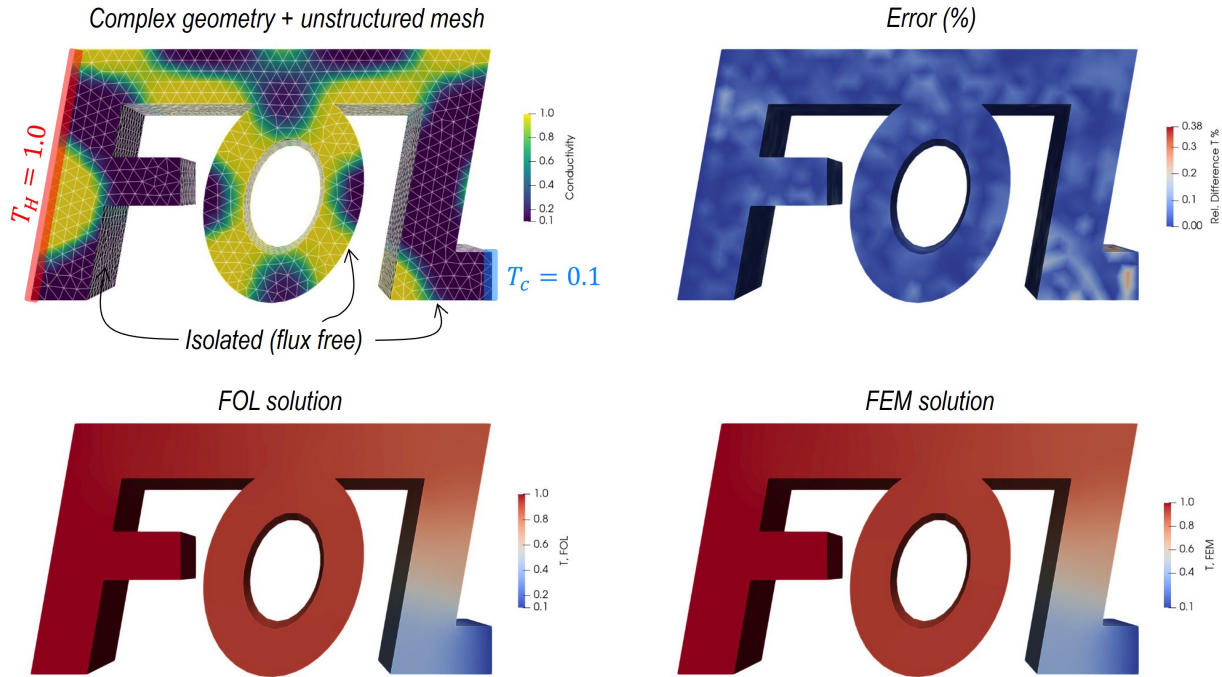


Figure 22: Comparison of FOL and FEM for a nonlinear PDE in a complex geometry.

5. Conclusion and outlooks

This work showcases a simple-to-use, data-free, physics-based neural operator technique for parametric learning of equations across arbitrarily shaped domains. The idea is to take any discretized parametric design space as an input layer and set the desired solution at a finite number of sensor points as the output layer. Next, the output and input will be used in the given set of governing physical equations while the boundary terms can be satisfied in a hard manner. Based on the proposed architecture, the current method can be coupled with any available numerical schemes. For the current work, we take advantage of the finite element

method and use the discretized version of the weak form or energy form of the problem. By using shape functions and their spatial derivatives, we avoid the need for automatic differentiation in constructing the physical loss functions, which enhances training efficiency.

The proposed methodology also ensures accurate solution-to-design sensitivities (output-to-input) by incorporating the stationarity of the residuals into the loss function (also known as Sobolev training). As a result, one can directly use the method to perform tasks in gradient-based optimization without any additional cost for adjoint-based sensitivity analysis. In particular cases, when optimization and parametric learning are not of interest, the method reduces to a matrix-free PDE solver, which requires much less memory space for calculations.

We applied our methodology to a steady-state thermal diffusion problem within a strongly heterogeneous domain (i.e., two-phase microstructure). Our findings demonstrate that even when considering a relatively high phase contrast, the method accurately predicts the temperature and flux profile. Moreover, thanks to the Sobolev training and the additional physical loss term for sensitivities, we performed a gradient-based topology optimization where an optimal design for the microstructure topology is discovered under given objective and constraint functions. By comparing calculation times and optimal solutions, we concluded that the FOL method can outperform classical adjoint-based techniques for gradient-based optimization.

A comprehensive comparison among various available numerical methods is not straightforward due to several reasons. Firstly, some of the newer methods, particularly those based on deep learning, are still under development. Secondly, depending on the application, dimensionality, computational resources, and implementation complexities, certain methods may prove more beneficial than others. Setting these aspects aside, a basic comparison between FEM, PINN, and FOL is presented in Table 6.

Table 6: Comparison of different approaches for solving PDEs.

	FEM	PINN	FOL
Implementing/Transferring codes	Hard (software specific)	Easy (only network evaluation)	Easy (only network evaluation)
Training time	- (doesn't apply)	Moderate-high (based on AD)	Moderate (based on shape functions)
Parametric learning	No	Yes (upon using extra inputs or branch net)	Yes
Order of derivations	Low (weak form)	High (unless using DEM or Mixed-PINN)	Low (weak form)
Handling complex geometries	Yes	Yes	Yes
Handling strong heterogeneity	Yes	Yes, by using Mixed PINN or domain decomp.	Yes
Data requirement	Only model param.	Only model param. no additional solution is required	Only model param. no additional solution is required
Main limitation	Comput. cost + discretization error	Training cost	discretization error
Main advantage	Accurate solutions for various PDEs	Fast eval. + no data is required	Fast eval. + no data is required

The main advantages of the current work are as follows: First, training the network in a data-free and parametric manner. Second, sensitivities are correctly captured based on Sobolev training. Third, the method can be utilized for fast forward prediction and inverse design, even when considering significant jumps in the solution field.

In future works, it is worth comparing the performance of the method against other neural operator techniques. The FOL framework also opens up new horizons for computational physics in various fields (e.g., mechanical and multiphysics problems [72, 28]). Combining the framework with autoencoders to achieve more flexibility in parameterization and handle arbitrary-shaped inputs is also of great interest, which is partially discussed in [70]. Finally, one is not limited to the FEM method to construct the loss terms in the proposed method; any other numerical schemes, especially spectral solvers, can also be utilized for faster speedup in multiscale computational systems.

Data Availability: The codes and data associated with this research are available upon request and will be published online following the official publication of the work.

Acknowledgements: The authors would like to thank the Deutsche Forschungsgemeinschaft (DFG) for the funding support provided to develop the present work in the project Cluster of Excellence “Internet of Production” (project: 390621612).

Author Statement: S.R.: Conceptualization, Supervision, Software, Writing - Review & Editing. R.N.A.: Conceptualization, Methodology, Software, Writing - Review & Editing. K. T.: Investigation, Software. A. M.: Software, Review & Editing. M. K.: Supervision, Review & Editing. M. A.: Funding, Supervision, Review & Editing.

Appendix A. Derivation of FEM residuals

In Section 2.1, we derived the weak form of the steady-state diffusion equation. Utilizing the standard finite element method, the temperature field T , conductivity field k as well as their first spatial derivatives, are approximated as

$$T = \sum N_i T_i = \mathbf{N}_e^T \mathbf{T}_e, \quad \nabla T = \sum B_i T_i = \mathbf{B}_e \mathbf{T}_e, \quad k = \sum N_i k_i = \mathbf{N}_e^T \mathbf{k}_e. \quad (\text{A.1})$$

Here, T_i and k_i are the nodal values of the temperature and conductivity field of node i of element e , respectively. Moreover, matrices \mathbf{N}_e and \mathbf{B}_e store the elemental shape functions and their spatial derivatives. For a quadrilateral 2D element, they are written as

$$\mathbf{N}_e^T = [N_1 \quad \cdots \quad N_4], \quad \mathbf{B}_e = \begin{bmatrix} N_{1,x} & \cdots & N_{4,x} \\ N_{1,y} & \cdots & N_{4,y} \end{bmatrix}, \quad (\text{A.2})$$

$$\mathbf{T}_e^T = [T_1 \quad \cdots \quad T_4], \quad \mathbf{k}_e^T = [k_1 \quad \cdots \quad k_4]. \quad (\text{A.3})$$

The notation $N_{i,x}$, and $N_{i,y}$ represent the derivatives of the shape function N_i with respect to the coordinates x and y , respectively. To compute these derivatives, we utilize the Jacobian matrix $\mathbf{J} = \partial \mathbf{X} / \partial \boldsymbol{\xi}$, a standard procedure in any finite element subroutine [76, 77]. Here, $\mathbf{X} = [x, y]$ and $\boldsymbol{\xi} = [\xi, \eta]$ represent the physical and parent coordinate systems, respectively. Finally, one can derive the so-called *discrete residual* form of the weak formulation in Eq. 6 as

$$\mathbf{r} = \sum \int_{\Omega_e} [\mathbf{B}_e]^T k [\mathbf{B}_e \mathbf{T}_e] dV - \int_{\Omega_t} [\mathbf{N}_e]^T k [\mathbf{B}_e \mathbf{T}_e] \mathbf{n} dS - \int_{\Omega_e} [\mathbf{N}_e]^T Q dV. \quad (\text{A.4})$$

The above formulation is shown for the 2D case, which is primarily reported in the results of this work. Extending this to 3D is straightforward and follows the standard FEM procedure exactly.

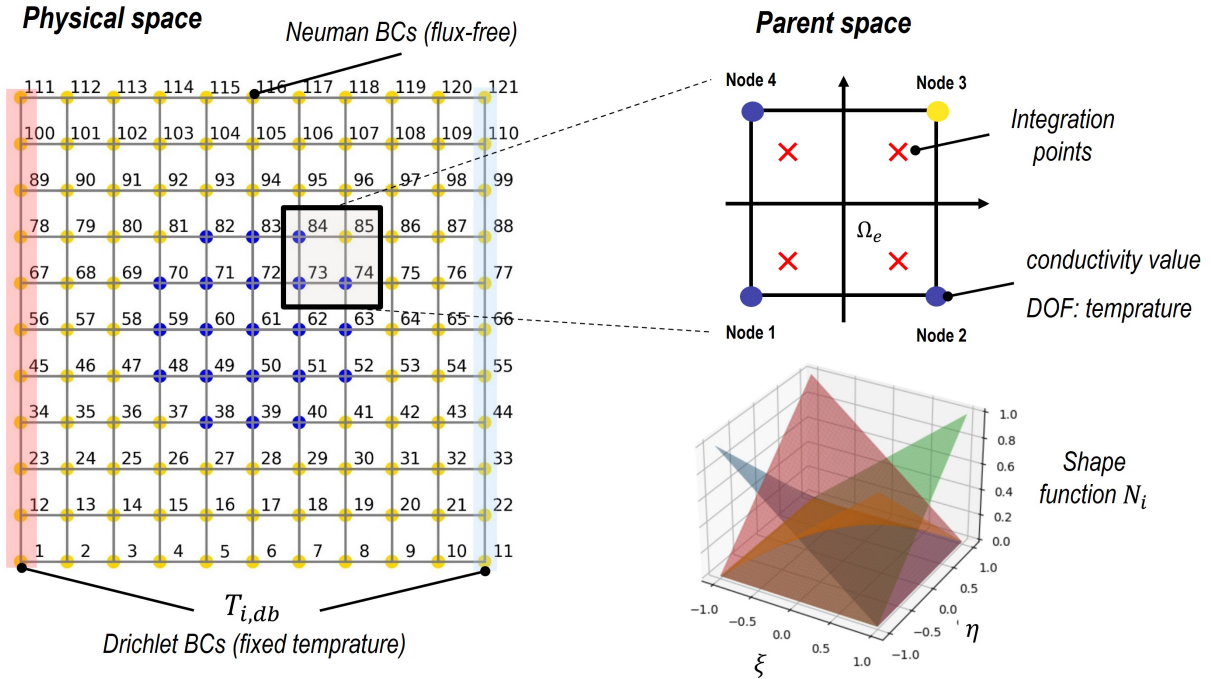


Figure A.23: The physical space and the parent space. Gaussian integration and shape functions are executed and defined specifically within the parent space.

Appendix B. Supplementary results

Appendix B.0.1. Additional results: influence of number of epochs on the performance of the FOL

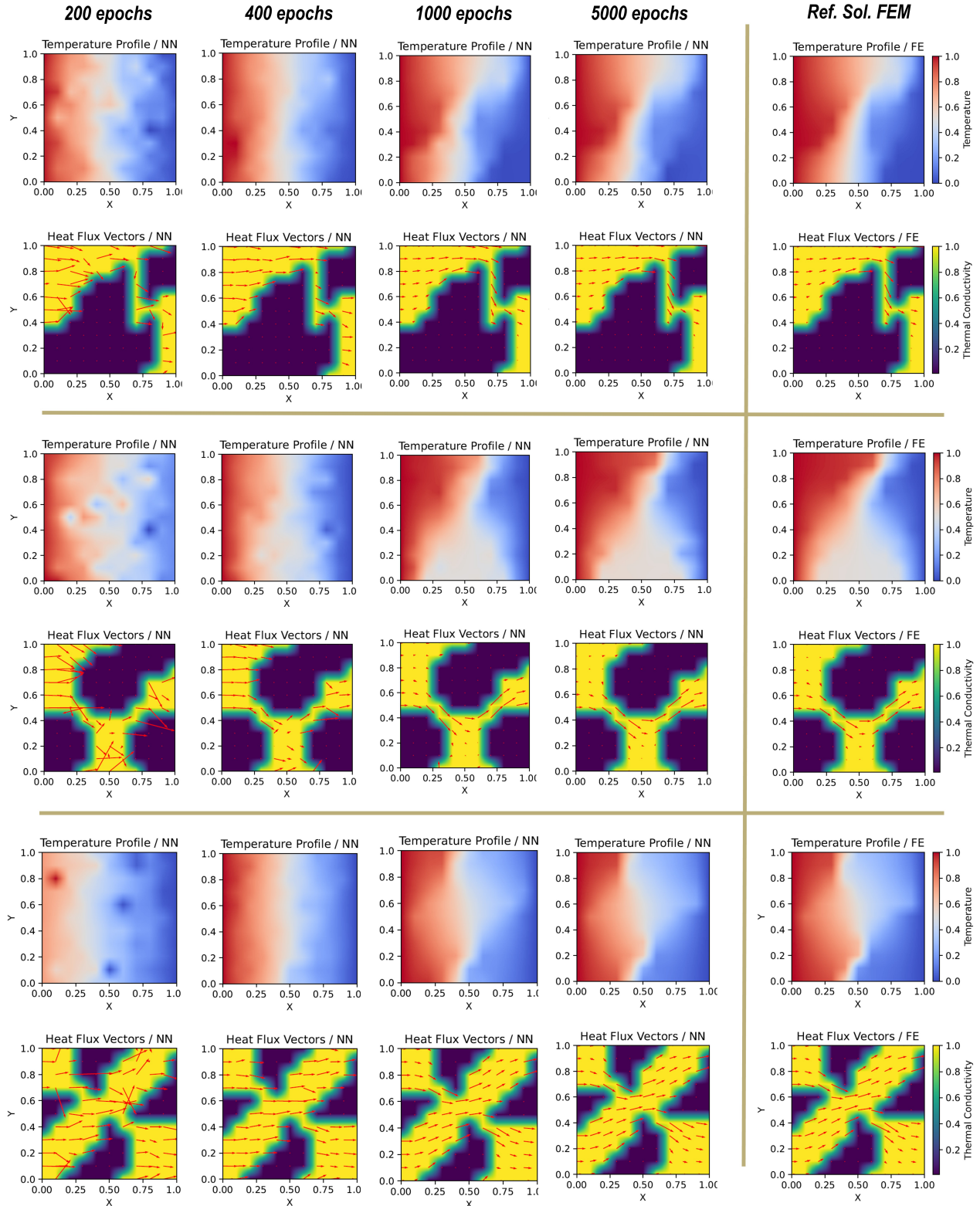


Figure B.24: Predictions of the trained FOL for different numbers of epochs.

Appendix B.0.2. Influence of activation functions

In Fig. B.25, we look into the influence of various choices for the activation function on the predictions. To avoid repetition, only the pointwise error for each choice of the activation function is shown in each row and column of Fig. B.25. Except for the linear case, which is an oversimplified case, the errors using other types of activation functions remain low.

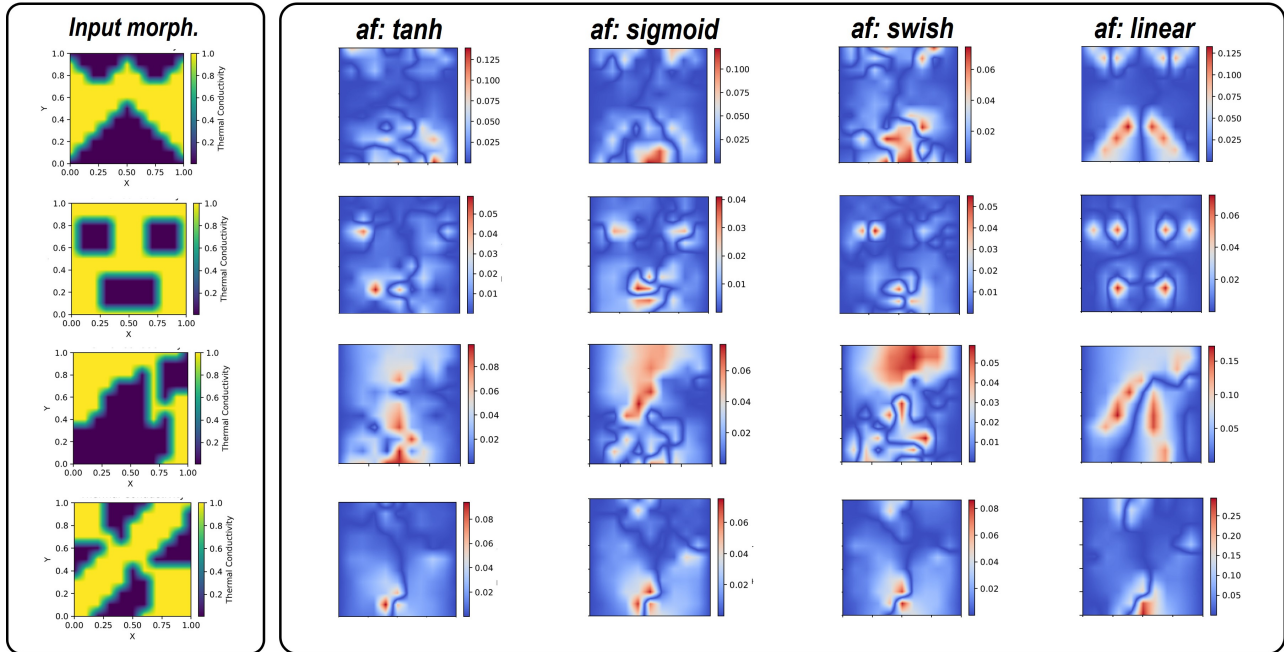


Figure B.25: Influence of the type of activation function on the obtained results.

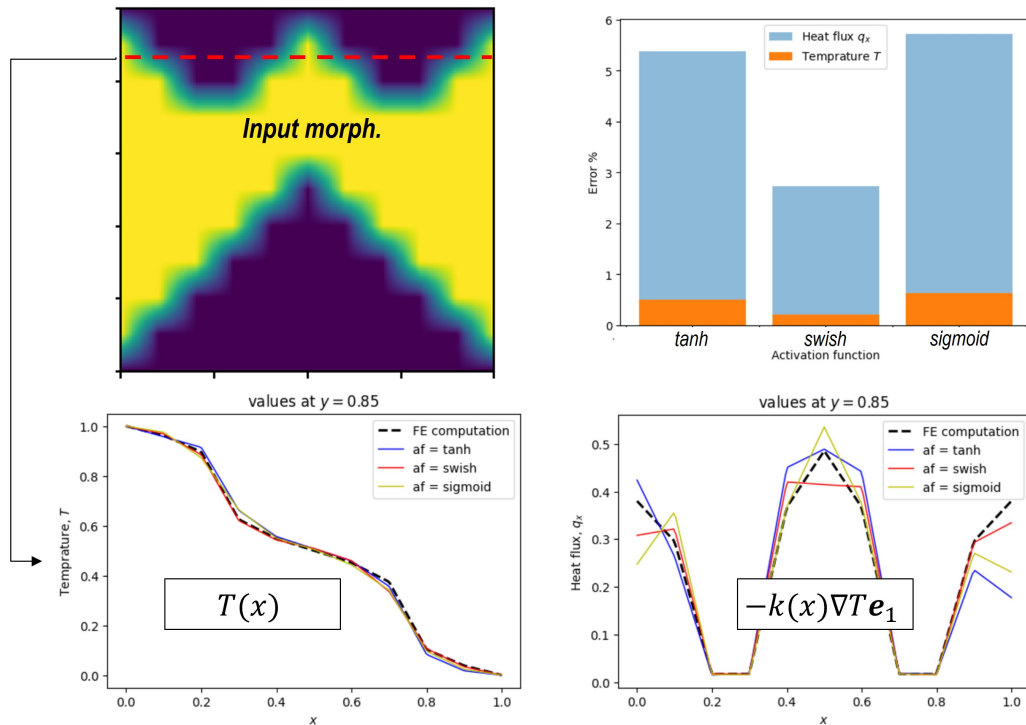


Figure B.26: Evaluation of averaged errors for different choice of activation functions.

In total, the tanh and swish functions showed the best performance. For a better and more quantitative comparison, the cross-section of the predictions and averaged errors are reported in Fig. B.26. To avoid repetition, the error values in this case are calculated based on $Err = \frac{|\langle T_{NN} \rangle - \langle T_{FE} \rangle|}{|\langle T_{FE} \rangle|} \times 100$, where we have $\langle T_{NN} \rangle = \frac{1}{N^2} \sum_i T_{NN}(i)$. This is motivated by the idea of homogenization, where we average the obtained temperature and heat flux to obtain the overall material properties. The lower this homogenized error is, the higher the accuracy will be for the homogenization of properties

Interestingly, the errors for the homogenized temperature are below 1%, which also holds for many other test cases not reported here. On the other hand, the average error for the flux in x-direction is higher, which is reasonable since we only predict the temperature profile and any slight fluctuations in the predicted temperature influence its spatial derivatives. The errors for the heat flux using the swish option are still acceptable and remain between 2% to 3%. One should note that ideas from mixed formulations, where we predict the heat flux as an output, can also be integrated with the current formulation to enhance the predictive ability of the neural network for higher-order gradients of the solutions (see investigations in [11, 78]).

References

- [1] Tobias Weinzierl. *The Pillars of Science*, pages 3–9. Springer International Publishing, Cham, 2021.
- [2] Thomas Bergs, Sascha Gierlings, Thomas Auerbach, Andreas Klink, Daniel Schraknepper, and Thorsten Augspurger. The concept of digital twin and digital shadow in manufacturing. *Procedia CIRP*, 101:81–84, 2021. 9th CIRP Conference on High Performance Cutting.
- [3] Salah A. Faroughi, Nikhil M. Pawar, Célio Fernandes, Maziar Raissi, Subasish Das, Nima K. Kalantari, and Seyed Kouros Mahjour. Physics-Guided, Physics-Informed, and Physics-Encoded Neural Networks and Operators in Scientific Computing: Fluid and Solid Mechanics. *Journal of Computing and Information Science in Engineering*, 24(4):040802, 2024.
- [4] Wing Kam Liu, Shaofan Li, and Harold S. Park. Eighty years of the finite element method: Birth, evolution, and future. *Archives of Computational Methods in Engineering*, 2022.
- [5] Hui Ruan, Shahed Rezaei, Yangyiwei Yang, Dietmar Gross, and Bai-Xiang Xu. A thermo-mechanical phase-field fracture model: Application to hot cracking simulations in additive manufacturing. *Journal of the Mechanics and Physics of Solids*, 172:105169, 2023.
- [6] Shahed Rezaei, Jacob Niikoi Okoe-Amon, Cerun Alex Varkey, Armin Asheri, Hui Ruan, and Bai-Xiang Xu. A cohesive phase-field fracture model for chemo-mechanical environments: Studies on degradation in battery materials. *Theoretical and Applied Fracture Mechanics*, 124:103758, 2023.
- [7] Francisco J. Montáns, Elías Cueto, and Klaus-Jürgen Bathe. *Machine Learning in Computer Aided Engineering*, pages 1–83. Springer International Publishing, Cham, 2023.
- [8] Mauricio Fernández, Shahed Rezaei, Jaber Rezaei Mianroodi, Felix Fritzen, and Stefanie Reese. Application of artificial neural networks for the prediction of interface mechanics: a study on grain boundary constitutive behavior. *Advanced Modeling and Simulation in Engineering Sciences*, 7:1–27, 2020.

- [9] Grace C. Y. Peng, Mark Alber, Adrian Buganza Tepole, William R. Cannon, Suvaranu De, Savador Dura-Bernal, Krishna Garikipati, George Karniadakis, William W. Lytton, Paris Perdikaris, Linda Petzold, and Ellen Kuhl. Multiscale modeling meets machine learning: What can we learn? *Archives of Computational Methods in Engineering*, 28:1017–1037, 2021.
- [10] Jaber Rezaei Mianroodi, Shahed Rezaei, Nima H Siboni, Bai-Xiang Xu, and Dierk Raabe. Lossless multi-scale constitutive elastic relations with artificial intelligence. *npj Computational Materials*, 8:1–12, 2022.
- [11] Shahed Rezaei, Ali Harandi, Ahmad Moeineddin, Bai-Xiang Xu, and Stefanie Reese. A mixed formulation for physics-informed neural networks as a potential solver for engineering problems in heterogeneous domains: Comparison with finite element method. *Computer Methods in Applied Mechanics and Engineering*, 401:115616, 2022.
- [12] M. Raissi, P. Perdikaris, and G.E. Karniadakis. Physics-informed neural networks: A deep learning framework for solving forward and inverse problems involving nonlinear partial differential equations. *Journal of Computational Physics*, 378:686–707, 2019.
- [13] M. Torabi Rad, A. Viardin, G.J. Schmitz, and M. Apel. Theory-training deep neural networks for an alloy solidification benchmark problem. *Computational Materials Science*, 180:109687, 2020.
- [14] Justin Sirignano and Konstantinos Spiliopoulos. Dgm: A deep learning algorithm for solving partial differential equations. *Journal of Computational Physics*, 375:1339–1364, 2018.
- [15] Stefano Markidis. The old and the new: Can physics-informed deep-learning replace traditional linear solvers? *Frontiers in Big Data*, 4, 2021.
- [16] Ameya D. Jagtap, Ehsan Kharazmi, and George Em Karniadakis. Conservative physics-informed neural networks on discrete domains for conservation laws: Applications to forward and inverse problems. *Computer Methods in Applied Mechanics and Engineering*, 365:113028, 2020.
- [17] Ameya D Jagtap and George Em Karniadakis. Extended physics-informed neural networks (xpinns): A generalized space-time domain decomposition based deep learning framework for nonlinear partial differential equations. *Communications in Computational Physics*, 28 (5):2002–2041, 2020.
- [18] Ben Moseley, Andrew Markham, and Tarje Nissen-Meyer. Finite basis physics-informed neural networks (fbpinns): a scalable domain decomposition approach for solving differential equations. *Advances in Computational Mathematics*, 2023.
- [19] Ehsan Haghghat, Maziar Raissi, Adrian Moure, Hector Gomez, and Ruben Juanes. A physics-informed deep learning framework for inversion and surrogate modeling in solid mechanics. *Computer Methods in Applied Mechanics and Engineering*, 379:113741, 2021.
- [20] Sifan Wang, Hanwen Wang, and Paris Perdikaris. On the eigenvector bias of fourier feature networks: From regression to solving multi-scale pdes with physics-informed neural networks. *Computer Methods in Applied Mechanics and Engineering*, 384:113938, 2021.

- [21] Levi McClenny and Ulisses Braga-Neto. Self-adaptive physics-informed neural networks using a soft attention mechanism. *arXiv preprint arXiv:2009.04544*, 2020.
- [22] Weinan E and Bing Yu. The deep ritz method: A deep learning-based numerical algorithm for solving variational problems. *Communications in Mathematics and Statistics*, 6, 2018.
- [23] E. Samaniego, C. Anitescu, S. Goswami, V.M. Nguyen-Thanh, H. Guo, K. Hamdia, X. Zhuang, and T. Rabczuk. An energy approach to the solution of partial differential equations in computational mechanics via machine learning: Concepts, implementation and applications. *Computer Methods in Applied Mechanics and Engineering*, 362:112790, 2020.
- [24] Jan N. Fuhg and Nikolaos Bouklas. The mixed deep energy method for resolving concentration features in finite strain hyperelasticity. *Journal of Computational Physics*, 451: 110839, 2022.
- [25] Fuzhen Zhuang, Zhiyuan Qi, Keyu Duan, Dongbo Xi, Yongchun Zhu, Hengshu Zhu, Hui Xiong, and Qing He. A comprehensive survey on transfer learning. *Proceedings of the IEEE*, 109:43–76, 2021.
- [26] Somdatta Goswami, Cosmin Anitescu, Souvik Chakraborty, and Timon Rabczuk. Transfer learning enhanced physics informed neural network for phase-field modeling of fracture. *Theoretical and Applied Fracture Mechanics*, 106:102447, 2020.
- [27] Chen Xu, Ba Trung Cao, Yong Yuan, and Günther Meschke. Transfer learning based physics-informed neural networks for solving inverse problems in engineering structures under different loading scenarios. *Computer Methods in Applied Mechanics and Engineering*, 405:115852, 2023.
- [28] Ali Harandi, Ahmad Moeineddin, Michael Kaliske, Stefanie Reese, and Shahed Rezaei. Mixed formulation of physics-informed neural networks for thermo-mechanically coupled systems and heterogeneous domains. *International Journal for Numerical Methods in Engineering*, page e7388.
- [29] Lu Lu, Pengzhan Jin, Guofei Pang, Zhongqiang Zhang, and George Karniadakis. Learning nonlinear operators via deeponet based on the universal approximation theorem of operators. *Nature Machine Intelligence*, 2021.
- [30] Zongyi Li, Nikola Kovachki, Kamyar Azizzadenesheli, Burigede Liu, Kaushik Bhattacharya, Andrew Stuart, and Anima Anandkumar. Fourier neural operator for parametric partial differential equations. 2021.
- [31] Stefan Hildebrand and Sandra Klinge. Comparison of neural fem and neural operator methods for applications in solid mechanics. 2023.
- [32] Sifan Wang, Hanwen Wang, and Paris Perdikaris. Learning the solution operator of parametric partial differential equations with physics-informed deeponets. *Science Advances*, 7 (40):eabi8605, 2021.
- [33] Seid Koric and Diab W. Abueidda. Data-driven and physics-informed deep learning operators for solution of heat conduction equation with parametric heat source. *International Journal of Heat and Mass Transfer*, 203:123809, 2023.

- [34] Yin hao Zhu, Nicholas Zabaras, Phaedon-Stelios Koutsourelakis, and Paris Perdikaris. Physics-constrained deep learning for high-dimensional surrogate modeling and uncertainty quantification without labeled data. *Journal of Computational Physics*, 394:56–81, 2019.
- [35] Han Gao, Luning Sun, and Jian-Xun Wang. Phygeonet: Physics-informed geometry-adaptive convolutional neural networks for solving parameterized steady-state pdes on irregular domain. *Journal of Computational Physics*, 428:110079, 2021.
- [36] Zhizhou Zhang and Grace X Gu. Physics-informed deep learning for digital materials. *Theoretical and Applied Mechanics Letters*, 11(1):100220, 2021.
- [37] Wei Li, Martin Z. Bazant, and Juner Zhu. Phase-field deepnet: Physics-informed deep operator neural network for fast simulations of pattern formation governed by gradient flows of free-energy functionals. *Computer Methods in Applied Mechanics and Engineering*, 416:116299, 2023.
- [38] Katiana Kontolati, Somdatta Goswami, George Em Karniadakis, and Michael D. Shields. Learning in latent spaces improves the predictive accuracy of deep neural operators. 2023.
- [39] Xiaoxuan Zhang and Krishna Garikipati. Label-free learning of elliptic partial differential equation solvers with generalizability across boundary value problems. *Computer Methods in Applied Mechanics and Engineering*, 417:116214, 2023.
- [40] Jan Niklas Fuhg, Arnav Karmarkar, Teeratorn Kadeethum, Hongkyu Yoon, and Nikolaos Bouklas. Deep convolutional ritz method: parametric pde surrogates without labeled data. *Applied Mathematics and Mechanics*, 44(7):1151–1174, 2023.
- [41] Pu Ren, Chengping Rao, Yang Liu, Jian-Xun Wang, and Hao Sun. Phycrnet: Physics-informed convolutional-recurrent network for solving spatiotemporal pdes. *Computer Methods in Applied Mechanics and Engineering*, 389:114399, 2022.
- [42] Xiaoyu Zhao, Zhiqiang Gong, Yunyang Zhang, Wen Yao, and Xiaoqian Chen. Physics-informed convolutional neural networks for temperature field prediction of heat source layout without labeled data. *Engineering Applications of Artificial Intelligence*, 117:105516, 2023.
- [43] Zhao Zhang, Xia Yan, Piyang Liu, Kai Zhang, Renmin Han, and Sheng Wang. A physics-informed convolutional neural network for the simulation and prediction of two-phase darcy flows in heterogeneous porous media. *Journal of Computational Physics*, 477:111919, 2023.
- [44] Derek Hansen, Danielle C. Maddix, Shima Alizadeh, Gaurav Gupta, and Michael W. Mahoney. Learning physical models that can respect conservation laws. *Physica D: Nonlinear Phenomena*, 457:133952, January 2024.
- [45] Toby R.F. Phillips, Claire E. Heaney, Boyang Chen, Andrew G. Buchan, and Christopher C. Pain. Solving the discretised neutron diffusion equations using neural networks. *International Journal for Numerical Methods in Engineering*, 124(21):4659–4686, 2023.
- [46] Joel Najmon and Andres Tovar. Evaluation of Neural Network-Based Derivatives for Topology Optimization. *Journal of Mechanical Design*, 146(7):071704, 2024.

- [47] Doksoo Lee, Lu Zhang, Yue Yu, and Wei Chen. Deep neural operator enabled concurrent multitask design for multifunctional metamaterials under heterogeneous fields. *Advanced Optical Materials*, 12(15):2303087, 2024.
- [48] Li Zheng, Siddhant Kumar, and Dennis M. Kochmann. Data-driven topology optimization of spinodoid metamaterials with seamlessly tunable anisotropy. *Computer Methods in Applied Mechanics and Engineering*, 383:113894, 2021.
- [49] Qiyin Lin, Jun Hong, Zheng Liu, Baotong Li, and Jihong Wang. Investigation into the topology optimization for conductive heat transfer based on deep learning approach. *International Communications in Heat and Mass Transfer*, 97:103–109, 2018.
- [50] Junyan He, Charul Chadha, Shashank Kushwaha, Seid Koric, Diab Abueidda, and Iwona Jasiuk. Deep energy method in topology optimization applications. *Acta Mechanica*, 234, 2023.
- [51] Aaditya Chandrasekhar and Krishnan Suresh. Tounn: Topology optimization using neural networks. *Structural and Multidisciplinary Optimization*, 63(3):1135–1149, 2021.
- [52] Zeyu Zhang, Yu Li, Weien Zhou, Xiaoqian Chen, Wen Yao, and Yong Zhao. Tonr: An exploration for a novel way combining neural network with topology optimization. *Computer Methods in Applied Mechanics and Engineering*, 386:114083, 2021.
- [53] Jonas Zehnder, Yue Li, Stelian Coros, and Bernhard Thomaszewski. Ntopo: Mesh-free topology optimization using implicit neural representations. 2021.
- [54] Rebekka V. Woldseth, Niels Aage, J. Andreas Bærentzen, and Ole Sigmund. On the use of artificial neural networks in topology optimisation. *Structural and Multidisciplinary Optimization*, 65, 2022.
- [55] Raphael T Haftka. Simultaneous analysis and design. *AIAA journal*, 23(7):1099–1103, 1985.
- [56] Zhizhou Zhang, Jeong-Ho Lee, Lingfeng Sun, and Grace X Gu. Weak-formulated physics-informed modeling and optimization for heterogeneous digital materials. *PNAS Nexus*, 3(5):pgae186, 2024.
- [57] Saviz Mowlavi and Ken Kamrin. Topology optimization with physics-informed neural networks: application to noninvasive detection of hidden geometries. 2023.
- [58] Steffen Tillmann, Daniel Hilger, Norbert Hosters, and Stefanie Elgeti. Shape-optimization of extrusion-dies via parameterized physics-informed neural networks. *PAMM*, 23(4):e202300203, 2023.
- [59] Hyogu Jeong, Chanaka Batuwatta-Gamage, Jinshuai Bai, Yi Min Xie, Charith Rathnayaka, Ying Zhou, and YuanTong Gu. A complete physics-informed neural network-based framework for structural topology optimization. *Computer Methods in Applied Mechanics and Engineering*, 417:116401, 2023.
- [60] Nikolaos N. Vlassis and WaiChing Sun. Sobolev training of thermodynamic-informed neural networks for interpretable elasto-plasticity models with level set hardening. *Computer Methods in Applied Mechanics and Engineering*, 377:113695, 2021.

- [61] Hwijae Son, Jin Woo Jang, Woo Jin Han, and Hyung Ju Hwang. Sobolev training for physics informed neural networks. *arXiv preprint arXiv:2101.08932*, 2021.
- [62] Vsevolod I Avrutskiy. Enhancing function approximation abilities of neural networks by training derivatives. *IEEE transactions on neural networks and learning systems*, 32(2): 916–924, 2020.
- [63] Wojciech M Czarnecki, Simon Osindero, Max Jaderberg, Grzegorz Swirszcz, and Razvan Pascanu. Sobolev training for neural networks. *Advances in neural information processing systems*, 30, 2017.
- [64] Nikan Doosti, Julian Panetta, and Vahid Babaei. Topology optimization via frequency tuning of neural design representations. In *Proceedings of the 6th Annual ACM Symposium on Computational Fabrication*, pages 1–9, 2021.
- [65] Kyuwon Lee, Cheolwoong Kim, and Jeonghoon Yoo. Topology optimization for self-adjoint problems using neural network-based analysis and design. *Available at SSRN 4711477*.
- [66] Shahed Rezaei, Armin Asheri, and Bai-Xiang Xu. A consistent framework for chemo-mechanical cohesive fracture and its application in solid-state batteries. *Journal of the Mechanics and Physics of Solids*, 157:104612, 2021.
- [67] Reza Najian Asl and Kai-Uwe Bletzinger. The implicit bulk-surface filtering method for node-based shape optimization and a comparison of explicit and implicit filtering techniques. *Structural and Multidisciplinary Optimization*, 66(5):111, 2023.
- [68] J Kiendl, R Schmidt, R Wüchner, and K-U Bletzinger. Isogeometric shape optimization of shells using semi-analytical sensitivity analysis and sensitivity weighting. *Computer Methods in Applied Mechanics and Engineering*, 274:148–167, 2014.
- [69] Daniel A White, Mark L Stowell, and Daniel A Tortorelli. Topological optimization of structures using fourier representations. *Structural and Multidisciplinary Optimization*, 58: 1205–1220, 2018.
- [70] Rasoul Najafi Koopas, Shahed Rezaei, Natalie Rauter, Richard Ostwald, and Rolf Lammering. Introducing a microstructure-embedded autoencoder approach for reconstructing high-resolution solution field from reduced parametric space. *arXiv preprint arXiv:2405.01975*, 2024.
- [71] J Ben Rosen. The gradient projection method for nonlinear programming. part ii. nonlinear constraints. *Journal of the Society for Industrial and Applied Mathematics*, 9(4):514–532, 1961.
- [72] Shahed Rezaei, Reza Najian Asl, Shirko Faroughi, Mahdi Asgharzadeh, Ali Harandi, Rasoul Najafi Koopas, Gottfried Laschet, Stefanie Reese, and Markus Apel. A finite operator learning technique for mapping the elastic properties of microstructures to their mechanical deformations. 2024.
- [73] Yusuke Yamazaki, Ali Harandi, Mayu Muramatsu, Alexandre Viardin, Markus Apel, Tim Brepols, Stefanie Reese, and Shahed Rezaei. A finite element-based physics-informed operator learning framework for spatiotemporal partial differential equations on arbitrary domains. 2024.

- [74] James Bradbury, Roy Frostig, Peter Hawkins, Matthew James Johnson, Chris Leary, Dougal Maclaurin, George Necula, Adam Paszke, Jake VanderPlas, Skye Wanderman-Milne, and Qiao Zhang. JAX: composable transformations of Python+NumPy programs, 2018. URL <http://github.com/google/jax>.
- [75] Ehsan Haghghat and Ruben Juanes. Sciann: A keras/tensorflow wrapper for scientific computations and physics-informed deep learning using artificial neural networks. *Computer Methods in Applied Mechanics and Engineering*, 373:113552, 2021.
- [76] Klaus-Jurgen Bathe. *Finite Element Procedures*. Prentice Hall, Englewood Cliffs, NJ, 1st edition, 1996.
- [77] Thomas J. R. Hughes. *The Finite Element Method: Linear Static and Dynamic Finite Element Analysis*. Prentice Hall, Englewood Cliffs, NJ, 1st edition, 1987.
- [78] Shirko Faroughi, Ali Darvishi, and Shahed Rezaei. On the order of derivation in the training of physics-informed neural networks: case studies for non-uniform beam structures. *Acta Mechanica*, 234, 2023.